

Analysis of the Rhode Island Schumann Resonance Daily-Average Data

Robert Boldi^{1*}, Earle Williams², and Anirban Guha³

¹College of Sustainability Sciences and Humanities, Zayed University, Dubai, United Arab Emirates

²Parsons Laboratory, Massachusetts Institute of Technology, Cambridge Massachusetts, USA.

³Tripura University, Tripura, India.

ABSTRACT: A variety of putative influences upon Schumann resonance (SR) signals have been evaluated for the case of a 20 year record of measurements of two magnetic-field detectors and one electric-field detector located at West Greenwich Rhode Island, U.S.A. (71.6°W, 41.6°N). The detector-specific SR signals considered are the values of the parameters of the first six modes of an eight-mode, three-parameter, Lorentzian-line-shape model. The three parameters of the model are peak-center frequency, peak-quality factor, and peak intensity. This model was used to fit the daily-average Fourier-transform intensity spectra spanning the frequency range 3 Hz - 56 Hz. This results in 54 SR signals: 3 channels \times 6 modes / channel \times 3 parameters / mode.

We also computed an expected climatological-daily-average intensity spectra for each day and detector and fit these spectra to the above mentioned Lorentzian model. A linear regression of the observed parameters to the expected parameters finds that on average the climatological-daily-average data account for 35% of the variance ($R^2 = 0.35$) of the original SR series, with the best fits obtained for the Lorentzian-fit parameter peak-intensity where 70% of the variance of the original series was explained. Averaging across channels and parameters, the second and third modes were best modeled by the climatological-average data, explaining 50% of the total variance; all above results are significant at the $p \leq 0.001$ level.

We then subtracted the observed SR signals from the expected SR signals to generate residual SR signals. The residual SR time series display a systematic variation following the 11-year sunspot cycle. A linear regression of a nominal sunspot cycle with the residual time series averaged across all modes and channels, finds R^2 values for peak-center frequency = 0.59, peak-quality factor = 0.31, and peak intensity = 0.0. Averaging the residual time series across all modes and fit parameters, the sunspot cycle is found in each channel; the R^2 value for the E/W channel = 0.30, the R^2 for the N/S channel = 0.37, and the R^2 value for the E_z channel = 0.24. The sunspot-cycle pattern is strongest the mode 1 data ($R^2 = 0.48$) and decreases with increasing mode number; the R^2 for mode 6 = 0.15; all significant at the $p \leq 0.001$ level.

We then examined various putative influences upon these residual SR signals using a variety of techniques. The results indicate that direct measures of solar activity (e.g. sunspot number and area) most strongly influence peak-center frequency and peak-quality factor (median $R^2 = 0.50$) and less so the peak-intensity (median $R^2 = 0.02$). Terrestrial temperature signals (e.g. Ocean temperature anomalies) influence peak-intensity (median $R^2 = 0.15$) but not peak-center frequency nor peak-quality factor (median $R^2 = 0.01$).

We also examined the spectral characteristics of the residual SR signals. Both the peak-center frequency and peak-quality factor parameters, averaged over all of the modes and channels, display strong peaks at 11 years, 365 days, 180 days; in contrast, the peak-intensity parameter displays no similar features. This indicates that the values of the peak intensity parameter are well predicted by the global total lightning and the uniform-cavity model, while the peak-center frequency and peak-quality factor parameters are not. The values of these two parameters have a significant variation over the sunspot cycle unaccounted for by the global total lightning and the uniform-cavity model.

*Corresponding author, email: Robert.Boldi@zu.ac.ae, Postal address: PO Box 19282, Dubai, U.A.E.

INTRODUCTION

The intent of this paper is to determine the causes of the temporal fluctuations observed in the the Schumann resonance (SR) signals recorded at West Greenwich, Rhode Island, U.S.A. (71.6°W, 41.6°N). While previous authors (e.g. *Shvets et al* [2010], *Nickolaenko et al* [2011], *Williams and Satori* [2007], *Williams et al* [2006], and *Williams et al* [2010]) have used subsets of this data set, we here report on the data in its entirety in order to place earlier results in the context of the entire data set. We limit this analysis to those fluctuations occurring over periods of a day or longer; in a forthcoming paper we will examine the fluctuations occurring on periods of less than a day. The method we used to examine the temporal fluctuations is summarized as follows and is explained in detail in the subsequent sections.

We transformed the time series into two-minute-average Fourier-transform spectra and from these spectra computed the observed daily-average Fourier-transform spectra. Our nominal expectation is that these time series primarily represent the diurnal and annual variations in global lightning activity. In addition, we expect that the Fourier-transform intensity spectra of these time series, on short time periods (10's of seconds), are dominated by a few large-amplitude events. These events come from a variety of distances, and consequently, averaging the short term spectral intensities into a daily-average intensity spectra should reflect the diurnally-averaged distribution of distances to large events. We note that these spectra quite different from that obtained by computing a single Fourier transform of single time series 24 hours in duration.

We then computed the expected daily-average spectra and fit both the observed and expected spectra to an eight-mode, three-parameter Lorentzian spectral model. The three parameters of the model are peak-center frequency, peak-quality factor, and peak intensity. We retain the first 6 modes for analysis; this resulted in a set of 54 time series of fit parameters: 3 channels \times 6 modes / channel \times 3 parameters / mode. We subtracted the expected time series from the observed time series for each of the 54 time series; this produced the residual or unexplained variation in the SR signals. We compared these residuals with variety of putative influences using various methods. These steps are detailed below. Finally, we present a summary of our findings and conclusions.

THE RHODE ISLAND TIME SERIES

The SR signals studied here originated as three independent time series, each generated by one of three independent recording systems operating at a sampling rate of 350 Hz (during 1992 – 2006) and at 4 kHz (from 2006 – present). These detectors sample the vertical electric field and the North/South and East/West components of the horizontal magnetic field as described in *Heckman et al* [1998].

Data processing began by sliding a 15-second-wide Hann window over the data, if the data in the window were complete, had no clipped values, and had a RMS value that was within nominal limits, then the data were accepted as valid. During periods of background noise at Rhode Island, when the noise was characterized as a set of line-interferences, this Hann window was increased to 30 seconds to improve the spectral resolution and assist in detecting and removing the line interferences.

Of the approximately 7,000 days in the study period, we obtained approximately 3,000 days of data, with 600 runs of good data averaging 5 days in length. Some of the data breaks were due to long periods of local anthropogenic noise causing the time series and spectra to fail the various data quality checks, and some breaks in the data were to instrumental failures of various types (mostly caused by nearby lightning strikes).

OBSERVED DAILY-AVERAGE SPECTRUM

For each of the valid 15-second or 30-second time series, we first compute a discrete Fourier transform spectrum as shown in Equation 1.

$$X[k] = \frac{T}{N} \sum_{n=0}^{N-1} x[n] e^{-i \frac{2\pi}{N} nk}, k \in Z[0 \dots \frac{N}{2}] \quad (1)$$

Since $X[k]$ is complex, we form the intensity spectrum as the modulus of $X[k]$, i.e $I[k] = |X[k]| = X^*[k] \cdot X[k]$. The time-series data window was advanced 1/3 of the total window length after each each Fourier-transform was processed. These 15-second intensity spectra were averaged into two-minute spectra and, provided there were more than 30-seconds of valid data in the two-minute interval, we retained those two-minute spectrum that passed some further data-quality checks based on the amount of narrow-band interferences and the amount of impulsive local noise.

We then constructed the daily-average Fourier-transform spectra by averaging the two-minute average intensity spectra provided that there were at least 9-hourly averages in the day.

FITTING SPECTRA TO A MODEL

These spectra are then characterized with a Lorentzian line shape model using three parameters (peak-center frequency, peak intensity, and peak-quality factor) and 8-modes covering the frequency range 3 Hz – 56 Hz as in Eq. 7 of *Sentman* [1987]:

$$P[f; (P_n, f_n, \Delta f_n); N] = \sum_{n=1}^N \frac{P_n}{1 + \left[2 \left(\frac{f-f_n}{\Delta f_n} \right) \right]^2}, \quad (2)$$

where N is the number of modes used (8 in our case), P_n is the peak intensity at the peak-center frequency f_n , and Δf_n is the full-width-at-half-maximum of P_n . Defining a peak-quality factor as $Q_n = f_n / \Delta f_n$ we arrive at an equivalent formulation:

$$P[f; (P_n, f_n, Q_n); N] = \sum_{n=1}^N \frac{P_n}{1 + [2Q_n(\frac{f}{f_n} - 1)]^2}. \quad (3)$$

As modes 7 and 8 of the model were affected by a 60 Hz notch filter present in the recording system, we retained the fits to the first six modes for analysis representing 6×3 or 18 parameters per spectrum; since we have three spectra per day, this results in a total of 54 daily-time series. We can then use the three parameter symmetric Lorentzian line model as a useful method to characterize the shape of the spectra and consider changes in line shape parameters as the starting point for our analysis.

An example of a daily-average spectrum is shown in Figure 1 for 8 November, 2006. This Figure shows the individual Lorentzian line shapes in red, the sum of the individual modes in green, and the input data in black. Data rejected as noise is shown in orange. The values of the fit parameters are shown along the bottom of the Figure. We note that due to line interferences using the mean absolute error as the fit criterion produced fits that were visually less influenced by the line interferences.

THE EXPECTED DAILY-AVERAGE SPECTRUM

The computation of the expected daily-average spectra requires (1) the uniform cavity model of *Wait* [1996], *Jones* [1967], and *Ishaq and Jones* [1977] parameterized as in *Huang* [1998] and (2) the global lightning activity as a function of distance and direction to Rhode Island. The method used is as follows:

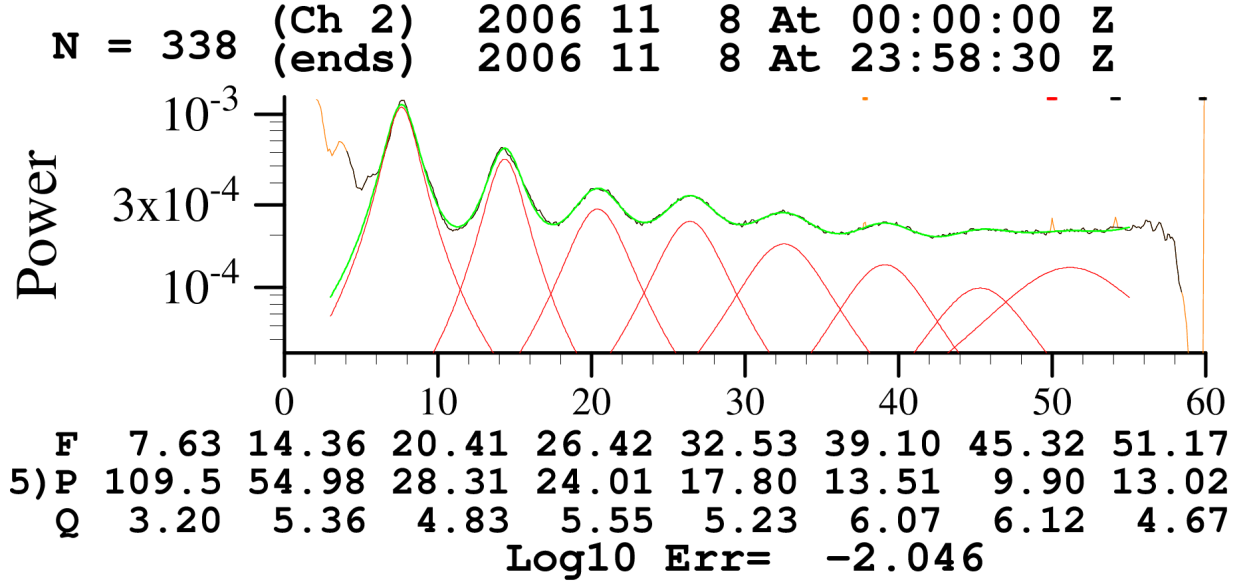


Figure 1: Observed E_Z daily-average spectrum for 8 November, 2006. Horizontal X axis is frequency (Hz). Red peaks are the individual Lorentzian peaks, green line is the sum of the Lorentzian peaks, and the black like is the observed data, and data ignored for various reasons are shown in orange. The values of the fit parameters are shown in bold across the bottom of the figure.

The uniform cavity, normal mode model

A lightning discharge causes an EM wave to be transmitted. The equations for the vertical electric field E_z and the horizontal magnetic field H_ϕ are given by Wait, Jones, and Ishaq (above) as:

$$E_z(\omega, \theta) = i \cdot I(\omega) ds \cdot \frac{\nu(\omega)(\nu(\omega) + 1) P_{\nu(\omega)}^0(-\cos \theta)}{4a^2 \epsilon_0 \omega h \sin(\pi \nu(\omega))} \quad (4)$$

and

$$H_\phi(\omega, \theta) = -I(\omega) ds \cdot \frac{P_{\nu(\omega)}^1(-\cos \theta)}{4ah \sin(\pi \nu(\omega))} \quad (5)$$

where $P_{\nu(\omega)}^0(x)$ and $P_{\nu(\omega)}^1(x)$ are the associated Legendre functions of the first kind, $I(\omega)ds$ is the current moment of the source, which we assume is a constant. The variables a and h are the radius of the Earth and the height of the ionosphere (80 km), and θ is the angular distance between the source and receiver ($0 - \pi$). The quantity $\nu(\omega)$ describes the propagation and dissipative characteristics of the atmosphere and was computed as in Eqs. 2.30 – 2.33 of Huang [1998] in which $f = \omega/2\pi$, and k is the wavenumber.

$$\nu(f) \cdot (\nu(f) + 1) = (kaS)^2 \quad [2.30]$$

$$S = \frac{C}{V} - i \left(5.49 \frac{\alpha}{f} \right) \quad [2.31]$$

$$\frac{C}{V} = 1.64 - 0.1759 \ln f + 0.01791 \ln^2 f \quad [2.32]$$

$$\alpha = 0.063 f^{0.64} \quad [2.33]$$

Values of $E_z(\omega, \theta)$ and $H_\phi(\omega, \theta)$ were computed at 0.1 Hz intervals from 1.0 Hz to 60 Hz and in 0.1

Mm intervals from 0.1 Mm to 20Mm. These values are used to construct the intensity spectra as a function of distance to the source for the three field detectors.

Global lightning: LIS/OTD derived LRTC and HRAC data sets

Using the climatological-daily LIS/OTD lightning data (Cecil [2014]), we constructed expected intensity spectra for each day with use of two LIS/OTD derived lightning data sets. The first set is the High Resolution Annual Climatology (HRAC) time series which is based on a $0.5^\circ \times 0.5^\circ$ grid. Each grid element is a time series of the climatological average daily lightning activity (*Flashes/km²/day*) for each day of the climatological year (365 values). The second set is the Low Resolution Time Series (LRTS). This data set is based on a $2.5^\circ \times 2.5^\circ$ grid, each grid element contains time series of the daily lightning activity for the period 1995 to 2012.

For each of these data sets, we first construct maps of daily global total lightning activity. Figure 2 shows these data for the case of the HRAC time series. The bottom-center panel of this map represents the normalized lightning activity observed by the omni-directional Electric field antenna (E_Z). We also create two other versions of these time series in which the activity of each grid element is weighted by the \sin^2 and the \cos^2 respectively of the bearing angle from Rhode Island to the grid location. These weights simulate the response of the North/South (N/S) aligned and East/West (E/W) aligned coils respectively and are shown in the left-hand and right-hand columns. Note that the bearing angle from Rhode Island to the central African lightning region is near the angle of maximum response of the N/S aligned coil and near the angle of minimum response of the E/W aligned coil.

Composite daily-average spectra

From these data (LRTC and HRAC) we then construct daily maps of lightning activity as a function of distance from Rhode Island weighted by the angular response of the detectors. The top row of Figure 2 shows the annual lightning activity based on the HRAC data set. The data shown are proportional to the square of the sine and cosine respectively and are shown in the top-left panel (N/S channel) and the top-right panel (E/W channel).

For each source bin ($0.5^\circ \times 0.5^\circ$ latitude/longitude) we multiply the pre-computed values of $E_z(\omega, \theta)$ and $H_\phi(\omega, \theta)$ by the activity (Flashes / day) and multiply by the bearing-angle weights (\cos^2 and \sin^2 for the E/W and N/S channels as appropriate. We then build a composite (average) intensity spectrum by summing the distance specific, bearing angle specific theoretical spectra together. Finally, we characterize this spectrum using the same Lorentzian line-fit model as was used to fit the observed spectra. An example of an expected daily-average spectrum is shown in Figure 3.

This composite, daily-average intensity spectra should resemble the observed daily-average spectra obtained by one of the three detectors: E/W magnetic, N/S magnetic and omni-directional E_Z . This procedure can be thought of as creating a nominal, base-line spectra that can be used when considering long-term averages, although we recognize it might be unsuitable when considering time periods less than a day.

RESIDUAL SR TIME SERIES

For each of the 54 SR time series, we subtracted the expected value of the parameter in question from the observed value. We did this using both the HRAC and the LRTS data sets. Perhaps surprisingly, the HRAC (daily climatological) data set outperformed the LRTS data set in that the HRAC data provided a better fit to the observed data than did the LRTS. This may be primarily due to the fact that the LRTS data is restricted to $\pm 40^\circ$ while the HRAC data spans $\pm 75^\circ$, as shown in Figure 4.

A sample of the fits of the HRAC and LRTS data to the observed data can be seen in Figures 5, 6, 7 that show the fits of F, I, and Q parameters for the HRAC and LRTS of the E/W channel, mode 1. In these

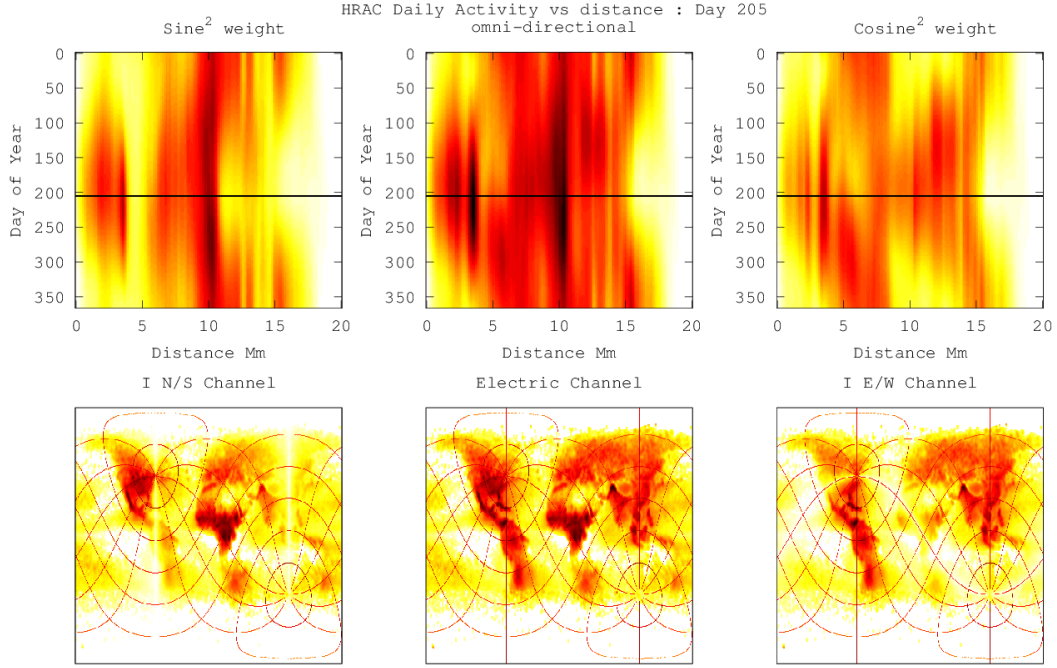


Figure 2: Top Row: Distribution of lightning activity vs distance from Rhode Island (horizontal axis) and day-of-year (vertical axis). Black horizontal line shows day-of-year that is presented in bottom row. Bottom Row: Normalized map of lightning activity for day 205 of climatological year. Left Column: Sine^2 weighting (N/S Channel). Middle Column: Uniform weighting (Ez Channel). Right Column: Cosine^2 weighting (E/W Channel). Based on the LIS/OTD-AC lightning data. Lines of constant distance and direction from West Greenwich, Rhode Island are also shown.

Figures, the top plot shows the observed SR signals minus HRAC-model predictions vs Time for Frequency (Hz) for E/W Channel, Mode 1. The middle plot shows the observed, HRAC-model, and LRTS-model time series of Frequency (Hz) for E/W Channel, Mode 1. The bottom row shows two scatter-plots of Observed vs Expected values of the LRTS model (left plot) and the HRAC model (right plot). The two R^2 values presented on this figure, one for the LRTS model and one for the HRAC model, are listed in Tables 2 and 1, respectively as the entry E/W, F, Mode 1.

A summary of the performance of the HRAC and LRTS data sets are presented in Tables 1 and 2. Table 1 shows the R^2 values of the fits of the observed Schumann parameters to the HRAC-model predicted time series for the three channels (E/W, N/S and Ez) and the fitted parameters Frequency (F), Intensity (I), and the Quality-factor (Q). Plots of the data represented by the first row (Mode 1) are presented in the lower-right-hand plots of Figures 5 to 7. Bold-face entries are significant at greater than the 0.0001 (0.01%) level.

Table 2 show the same data for the LRTS data, and Table 3 shows the ratios of the HRAC-model R^2 values to the LRTS-model R^2 values of the fits of the observed parameters to the predicted time series for the three channels (E/W, N/S and Ez) and the fit parameters Frequency (F), Intensity (I), and the Quality-factor (Q). Based on the superior performance of the HRAC data in predicting the observed Schumann resonance time series, we use this data set to form the predicted daily-average spectra using the methods discussed next.

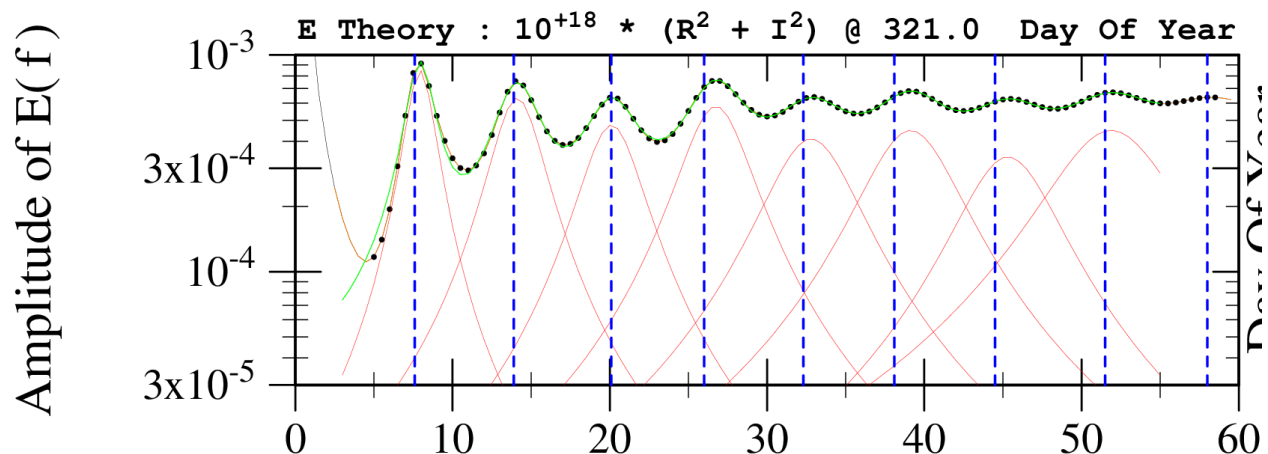


Figure 3: Expected E_Z spectra for 8 November, 2006 using uniform cavity model and LIS/OTD-AC lightning data. Horizontal X axis is frequency (Hz). Red peaks are the individual Lorentzian peaks, green line is the sum of the Lorentzian peaks, and the black like is the observed data. The vertical dashed blue lines are the nominal frequencies of the Schumann modes 1 – 9. This day corresponds to the same day as shown in Figure 1, i.e. 8 November, 2006.

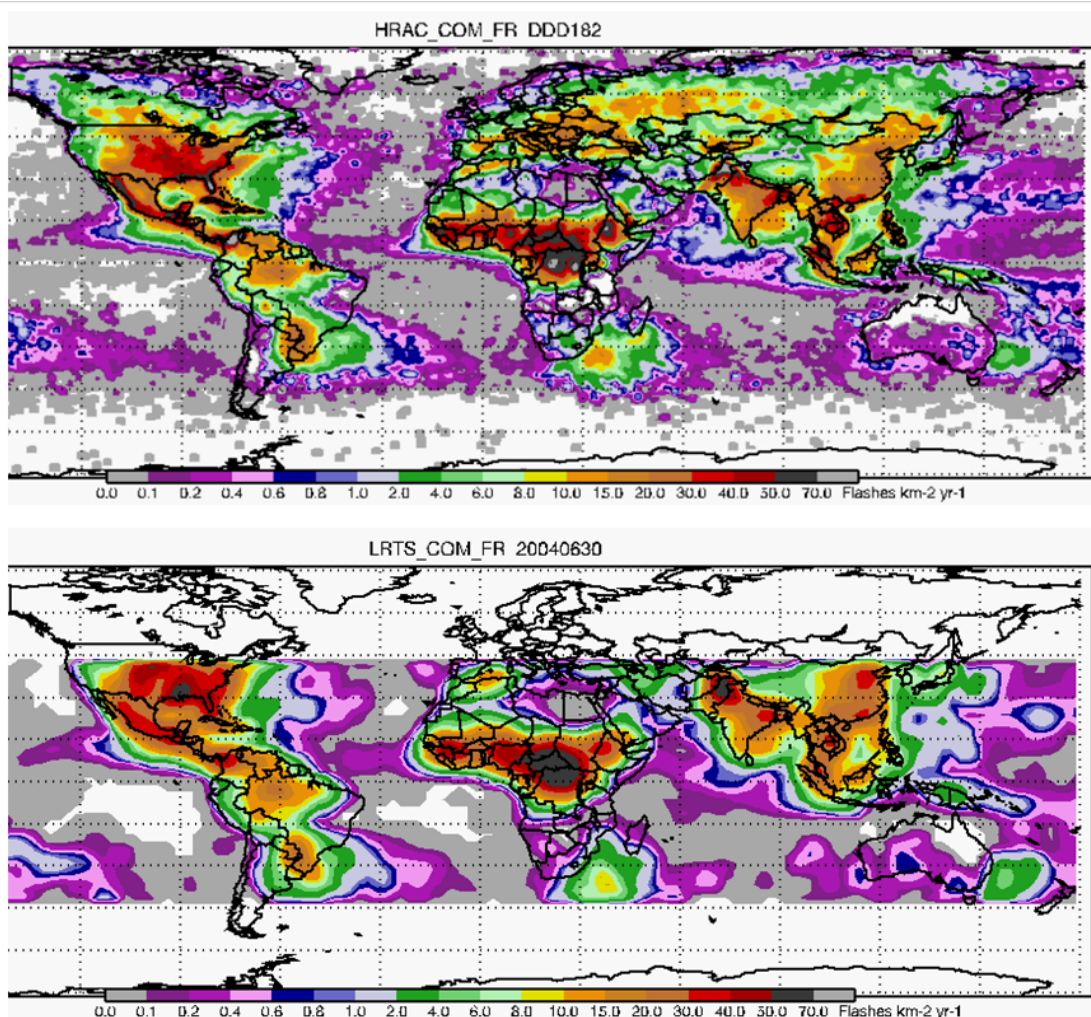


Figure 4: High Resolution Annual Climatology (HRAC) vs Low Resolution Time Series (LRTS). Top panel: HRAC data for day of year 182. Data span $\pm 75^\circ$ and are on a $0.5^\circ \times 0.5^\circ$ latitude/longitude grid. Bottom panel: LRTS for June 30, 2004. Data span $\pm 40^\circ$ and are on a $2.5^\circ \times 2.5^\circ$ latitude/longitude grid.

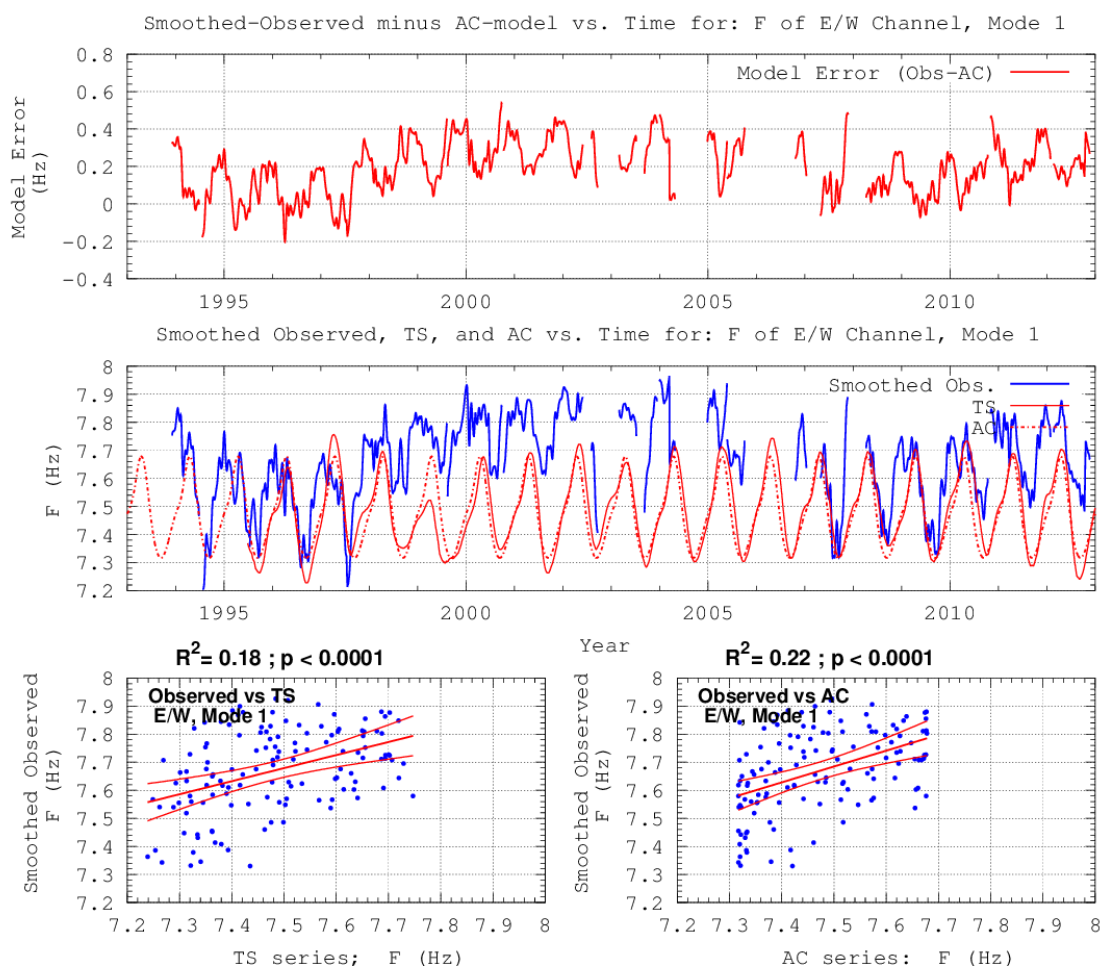


Figure 5: Top: Observed SR signals minus HRAC-model predictions vs Time for Frequency (Hz) for E/W Channel, Mode 1. Middle: Observed, HRAC-model, and LRTS-model time series of Frequency (Hz) for E/W Channel, Mode 1. Bottom: Scatter-plots of Observed vs Expected values of the LRTS model (left plot) and the HRAC model (right plot). The two R^2 values presented on this Figure, one for the LRTS model and one for the HRAC model, are listed in Tables 2 and 1, respectively as the entry E/W, F, Mode 1.

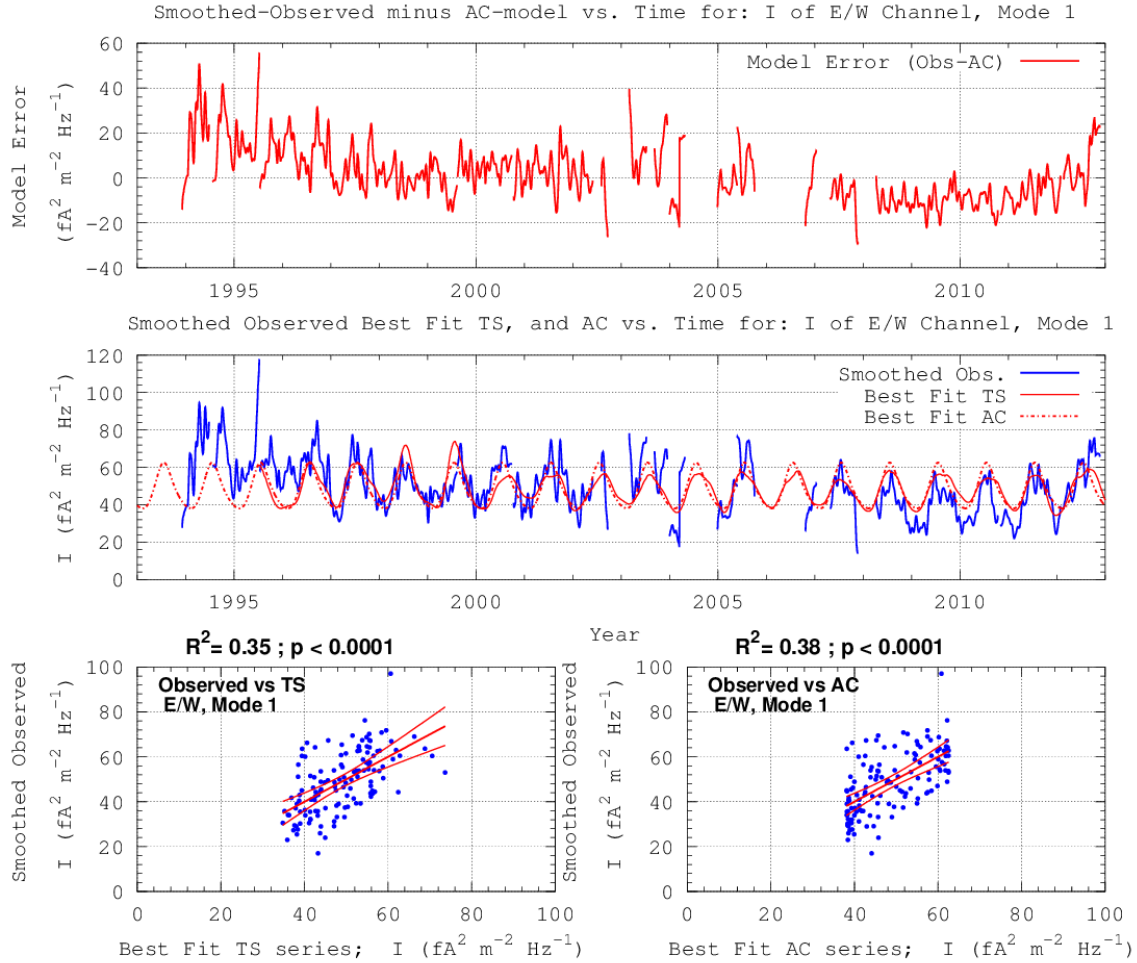


Figure 6: Top: Observed SR signals minus HRAC-model predictions vs time for Intensity (Normalized units) for E/W Channel, Mode 1. Middle: Observed, HRAC-model, and LRTS-model time series of Intensity (Normalized units) for E/W Channel, Mode 1. Bottom: Scatter-plots of Observed vs Expected values of the LRTS model (left plot) and the HRAC model (right plot). The two R^2 values presented on this Figure, one for the LRTS model and one for the HRAC model, are listed in Tables 2 and 1, respectively as the entry E/W, I, Mode 1.

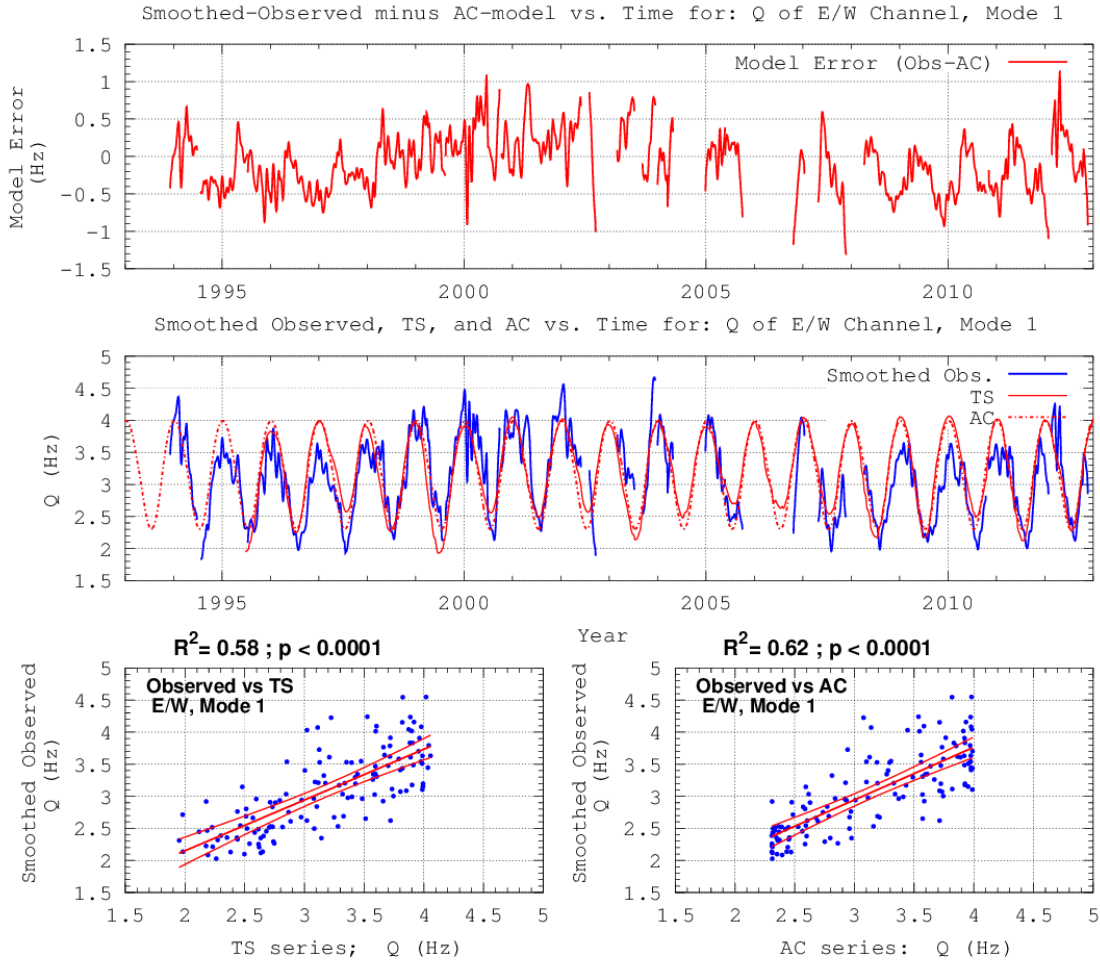


Figure 7: Top: Observed SR signals minus HRAC-model predictions vs time for Quality factor (Hz) for E/W Channel, Mode 1. Middle: Observed, HRAC-model, and LRTS-model time series of Quality factor (Hz) for E/W Channel, Mode 1. Bottom: Scatter-plots of Observed vs Expected values of the LRTS model (left plot) and the HRAC model (right plot). The two R^2 values presented on this figure, one for the LRTS model and one for the HRAC model, are listed in Tables 2 and 1, respectively as the entry E/W, Q, Mode 1.

Table 1: R^2 values of the fits of the observed Schumann parameters to the HRAC-model predicted time series for the three channels (E/W, N/S and Ez) and the fitted parameters Frequency (F), Intensity (I), and the Quality-factor (Q). Plots of the data represented by the first column (E/W) and first row (Mode 1) are presented in the lower-right-hand plots of Figures 5 to 7, having R^2 values of 0.22, 0.38, and 0.62: values near the median of all such values.

Mode	E/W			N/S			Ez			Median
	F	I	Q	F	I	Q	F	I	Q	
1	0.22	0.38	0.62	0.40	0.46	0.30	0.16	0.18	0.001	0.30
2	0.83	0.56	0.39	0.02	0.57	0.10	0.46	0.49	0.62	0.49
3	0.53	0.73	0.27	0.34	0.69	0.07	0.59	0.58	0.52	0.53
4	0.04	0.81	0.28	0.11	0.69	0.16	0.01	0.59	0.35	0.28
5	0.003	0.83	0.000	0.02	0.71	0.10	0.001	0.66	0.31	0.10
6	0.18	0.80	0.001	0.04	0.71	0.005	0.003	0.71	0.08	0.08
Median	0.20	0.76	0.28	0.08	0.69	0.10	0.09	0.59	0.33	
Median		0.39			0.23			0.40		0.35

Note: **Bold Face** values are significant at $p \leq 0.0001$

Table 2: R^2 values of the fits of the observed parameters to the LRTS based predicted time series for the three channels (E/W, N/S and Ez) and the fitted parameters Frequency (F), Intensity (I), and the Quality-factor (Q). Plots of the data represented by the first column (E/W) and the first row (Mode 1) are presented in the lower-left-hand plots of Figures 5 to 7, having R^2 values of 0.18, 0.35, and 0.58: values near the median of all such values.

Mode	E/W			N/S			Ez			Median
	F	I	Q	F	I	Q	F	I	Q	
1	0.18	0.35	0.58	0.42	0.34	0.29	0.14	0.14	0.004	0.29
2	0.77	0.53	0.34	0.05	0.67	0.11	0.36	0.45	0.57	0.45
3	0.43	0.66	0.31	0.43	0.75	0.06	0.47	0.51	0.45	0.45
4	0.05	0.76	0.24	0.15	0.76	0.15	0.01	0.56	0.18	0.18
5	0.002	0.75	0.01	0.003	0.79	0.02	0.006	0.62	0.19	0.02
6	0.09	0.74	0.01	0.02	0.77	0.02	0.02	0.67	0.09	0.09
Median	0.14	0.70	0.28	0.10	0.75	0.08	0.08	0.53	0.18	
Median		0.35			0.22			0.27		0.32

Note: **Bold Face** values are significant at $p \leq 0.0001$

Table 3: Ratio of the HRAC-model R^2 values to the LRTS-model R^2 values of the fits of the observed parameters to the predicted time series for the three channels (E/W, N/S and Ez) and the fit parameters Frequency (F), Intensity (I), and the Quality-factor (Q). Plots of the data represented by the first row (Mode 1) are presented in the lower two plots of Figures 5 to 7.

	E/W			N/S			Ez			
Mode	F	I	Q	F	I	Q	F	I	Q	Median
1	1.17	1.08	1.07	0.94	1.36	1.01	1.15	1.27	0.33	1.08
2	1.08	1.06	1.16	0.38	0.85	0.97	1.28	1.09	1.08	1.08
3	1.22	1.10	0.87	0.80	0.91	1.12	1.27	1.14	1.14	1.12
4	0.82	1.06	1.16	0.77	0.91	1.05	1.00	1.06	1.96	1.05
5	1.36	1.11	0.01	7.94	0.90	4.24	0.09	1.07	1.68	1.11
6	2.00	1.07	0.07	2.24	0.92	0.21	0.14	1.05	0.82	0.92
Median	1.20	1.08	0.97	0.87	0.91	1.03	1.07	1.08	1.11	
Median	1.08			0.93			1.08			1.07

GLOBAL LIGHTNING AND SPECTRAL INTENSITY

As a preliminary calculation, we regressed the observed peak intensity of each channel (c) and mode (m) $I_{c,m}$ with the LIS/OTD LRTS-based total-daily global lightning activity (Flashes / day). For the E/W and N/S magnetic data, the units of Intensity are ($\text{fA}^2 \text{ m}^{-2} \text{ Hz}^{-1}$), the E_Z channel is currently uncalibrated. Each regression is of the form

$$I_{c,m} = \alpha_{c,m} \cdot \sum_{lat,lon} F_{c,lat,lon}(\text{Total Lightning}_{lat,lon}) + \beta_{c,m} \cdot \quad (6)$$

The goodness of the fit ($R^2_{c,m}$) was also computed. In the above equation, $F_{c,lat,lon}()$ is a channel specific weighting function that accounts for the bearing-angle sensitivity of the E/W, and N/S detectors. The E_Z detector is omni-directional, and hence $F_{c,lat,lon}() \equiv 1$. Peak intensity of E/W and N/S channels ($I_{c,m}$) has units $\text{fA}^2 \text{ m}^{-2} \text{ Hz}^{-1}$, and total-daily global lightning has units M flashes per day. Figure 8 shows the time series of peak intensity ($I_{c,m}$) for the three channels (E/W, N/S, and E_Z) for Mode 1. Table 4 shows the results for all the modes examined (1 – 6). The median R^2 for all the modes and channels is approximately 0.6 which indicates that more than half of the total variance of the observed intensity is accounted for by the HRAC lightning data. This is a little higher than the amount of the total variance of the observed intensity explained by the intensities of the computed daily-average spectra.

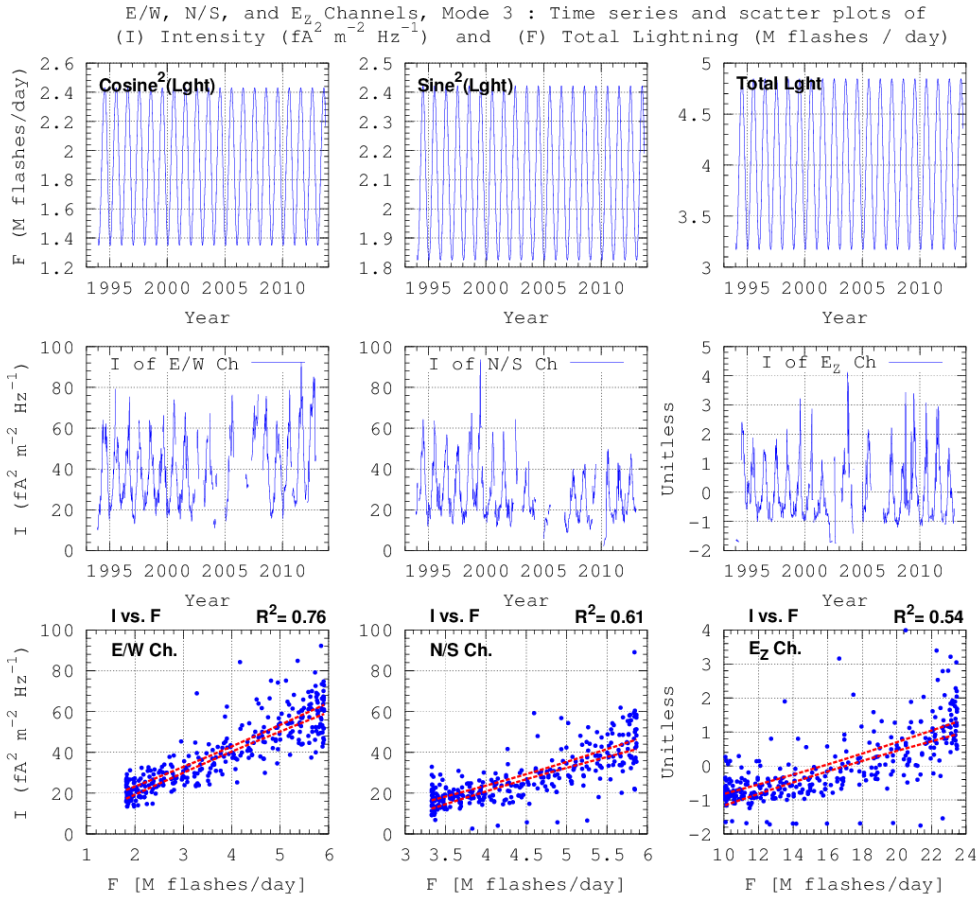


Figure 8: Regression of peak intensity of mode 3 with daily global total lightning from HRAC data. The lightning data was multiplied by \cos^2 , \sin^2 of the bearing angle to the source region prior to comparing with the Intensity data of the E/W and N/S channels respectively to simulate the angular sensitivities of these channels; c.f. Equation 6.

Table 4: Values of the parameters of the regressions of the observed Intensity ($\text{fA}^2 \text{ m}^{-2} \text{ Hz}^{-1}$) of channels E/W, N/S and E_z channels and modes 1 – 6 with the \cos^2 weighted, \sin^2 weighted, and unweighted values of the HRAC-total lightning (M flashes per day) time series respectively.

Mode	E/W			N/S			E_z		
	Slope α	Intercept β	R^2	Slope α	Intercept β	R^2	Slope α	Intercept β	R^2
1	5.17	30.99	0.26	20.03	-22.93	0.39	0.10	-1.67	0.23
2	7.47	19.22	0.53	11.11	-14.34	0.46	0.15	-2.47	0.50
3	10.19	0.86	0.76	11.60	-24.15	0.61	0.16	-2.56	0.54
4	8.25	-4.54	0.77	9.48	-22.62	0.59	0.16	-2.63	0.57
5	6.48	-2.73	0.79	8.35	-21.66	0.62	0.17	-2.78	0.63
6	5.51	-1.96	0.74	7.37	-20.66	0.64	0.17	-2.85	0.67
Median	6.97	-0.55	0.75	10.29	-22.14	0.60	0.16	-2.60	0.55

Note: All regressions significant at the $p \leq 0.001$ level.

ANALYSIS OF RESIDUAL SR SIGNALS.

The residual SR time series display a systematic variation following the 11-year sunspot cycle. We operationally defined the nominal sunspot cycle to be the 180 day normalized Gaussian weighted running average of the SSN, SSA, and R10 time series. A linear regression of a nominal sunspot cycle with the residual time series averaged across all modes and channels, finds R^2 values for peak-center frequency = 0.59, peak-quality factor = 0.31, and peak intensity = 0.0. Averaging the residual time series across all modes and fit parameters, the sunspot cycle is found in each channel; the R^2 value for the E/W channel is 0.30, the R^2 for the N/S channel is 0.37, and the R^2 value for the E_z channel is 0.24, all significant at the $p \leq 0.001$ level. The sunspot-cycle pattern is strongest the mode 1 data ($R^2 = 0.48$) and decreases with increasing mode number; the R^2 for mode 6 is 0.15;

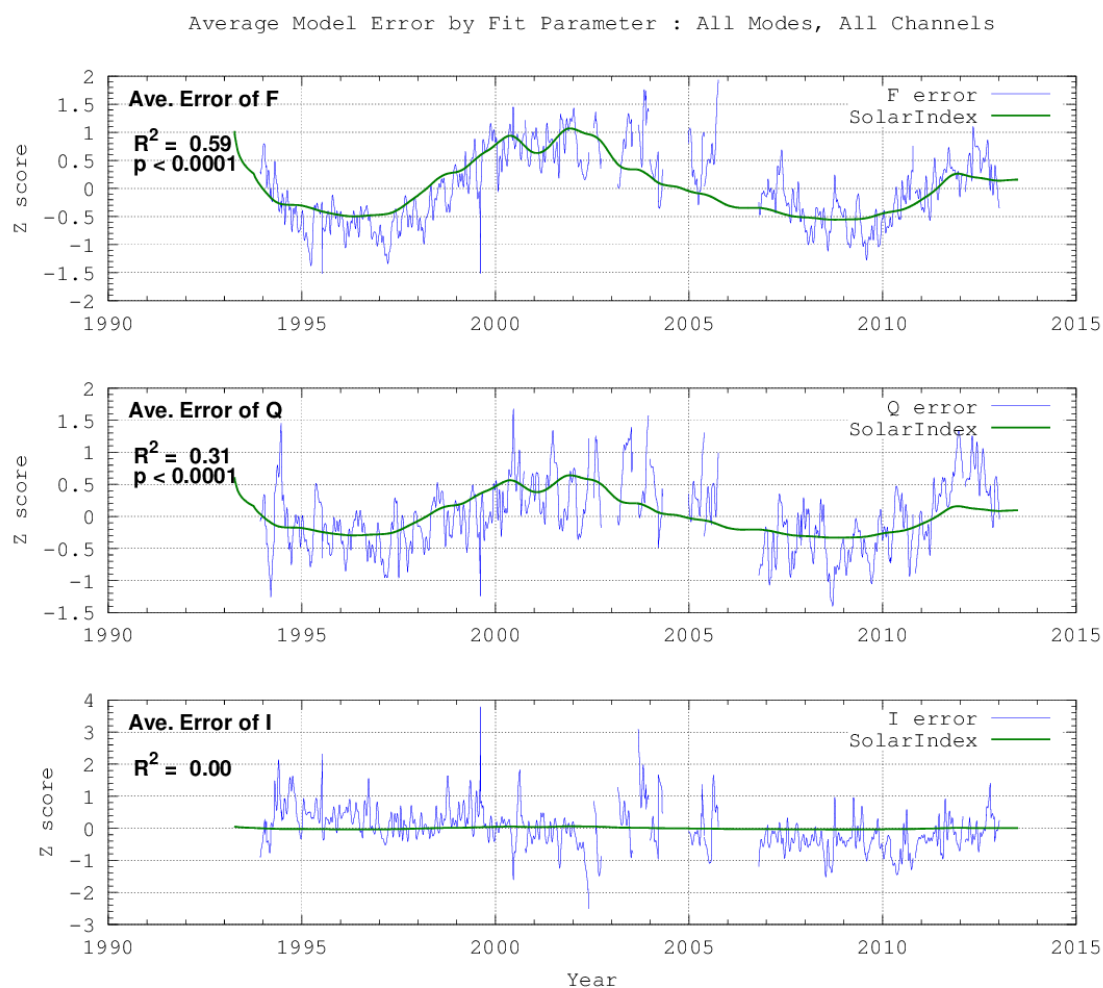


Figure 9: Average model error in the parameters F, I, and Q averaged over all resonant modes 1 – 6 and channels (E/W, N/S. and Ez).

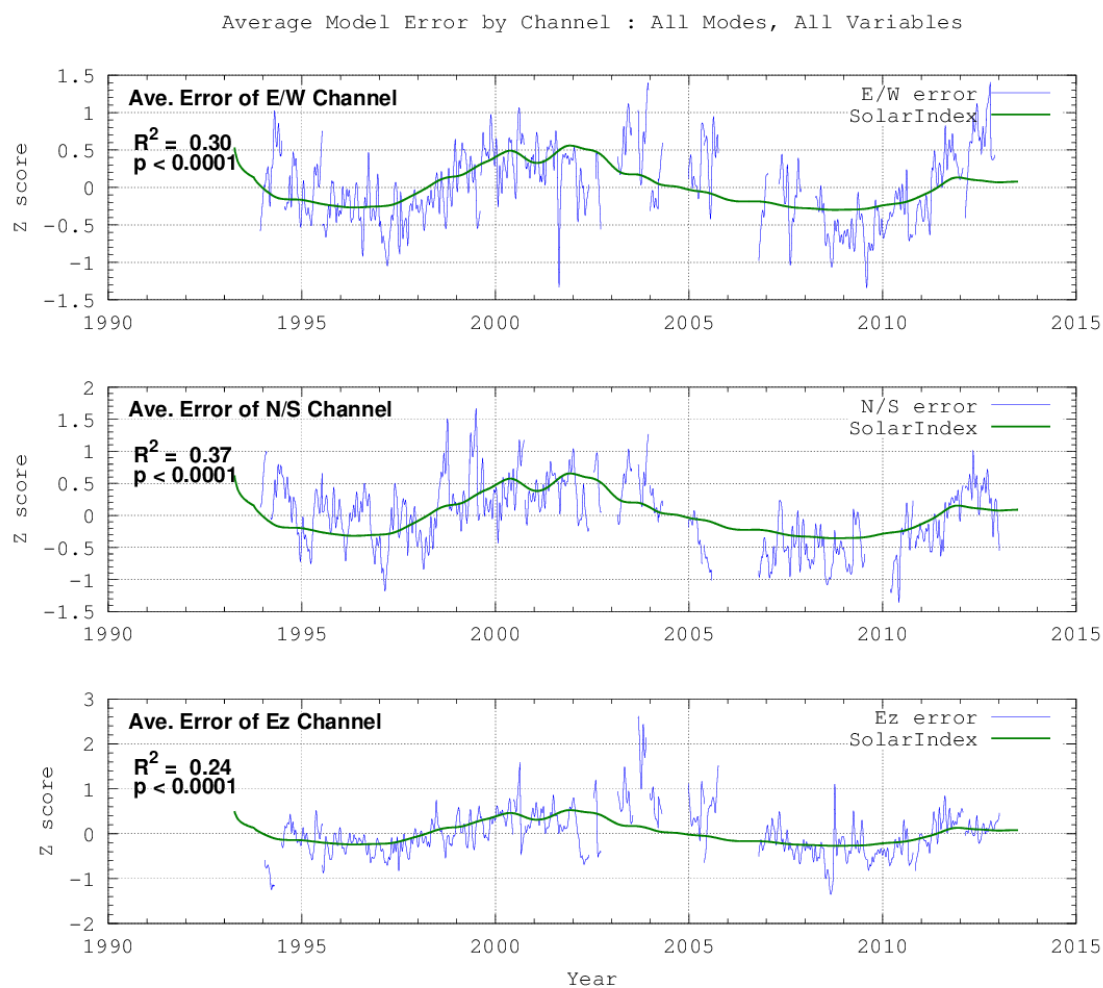


Figure 10: Average model error in the E/W, N/S and Ez channels averaged over all resonant modes 1 – 6 and Lorentzian ffit parameters (F, I, and Q).

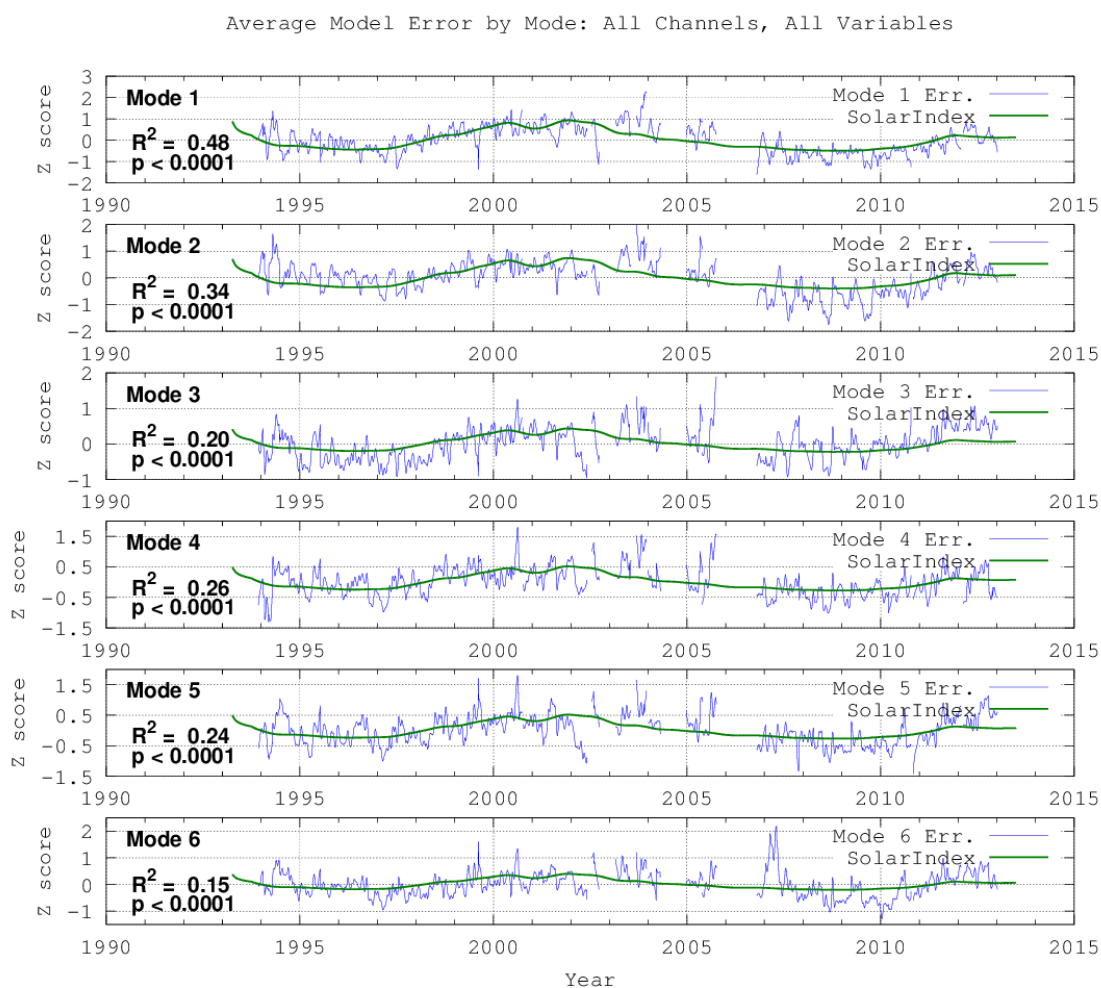


Figure 11: Average model error in the resonant modes 1 – 6 averaged over all Lorentzian fit parameters (F, I, and Q) and channels (E/W, N/S. and Ez).

PUTATIVE INFLUENCES UPON THE SR TIME SERIES

We wanted to test a variety of data sets that could, or have been postulated, to influence the SR signals. Hence, we acquired a large number of data sets for comparison with the SR data sets. In total, these six groups comprise 60 data sets. The putative influences considered fall into six groups; (1) six direct measures of solar activity, (2) five space-weather variables, (3) 19 terrestrial temperature anomaly data sets, (4) the LRTS and HRAC versions of the LIS/OTD global lightning data, (5) the GPCP global one-degree daily-precipitation data set, and (6) lunar and solar ephemeris data. In total, these six groups comprise 60 data sets. Specifically, the classes contain the following data sets.

Group 1. Direct measures of solar activity. This group includes six data sets representing observations of, and emissions from, the Sun. **[1.1] SSN:** SunSpot Number. We used two sources of sunspot numbers, (1) the Solar Influences Data Analysis Center, Royal Observatory of Belgium (*SIDC* [2013]), and the (2) U.S. Dept. of Commerce, NOAA, Space Environment Service Center (*NOAA/SESC* [2013]). We averaged the two data sets together to arrive at our sunspot number time series (SSN). **[1.2] SSA:** SunSpot faculaw Area. We used two sources for the sunspot area data. The first was a data set obtained from NOAA's Space Weather Prediction Center (*NOAA/SWPC*, [2013A]), the second was the The Solar Physics Group at NASA's Marshall Space Flight Center (*MSFC/SPG*, [2013]). We averaged the two data sources together to arrive at our sunspot total area time series (SSA). **[1.3/1.4] XRL, XRS:** GOES X-ray long/short-wavelength (0.1 nm – 0.8 nm)/(0.05 nm – 0.3 nm) irradiance ($\text{W}\cdot\text{m}^{-2}$). Both the XRL and XRS were obtained from NOAA's National Geophysical Data Center (*NOAA/NGDC* [2013]). **[1.5] R10:** Solar radio emissions at 10.7 cm wavelength, obtained from the U.S. Dept. of Commerce, NOAA, Space Environment Service Center (*NOAA/SESC* [2013]). **[1.6] TSI:** Total Solar Irradiance at 1 AU. Obtained from Physikalisch-Meteorologisches Observatorium Davos, World Radiation Centre (*PMOD/WRC* [2013]).

Group 2. Space-weather variables. This group includes five data sets representing conditions at or above the ionosphere; specifically: **[2.1] TPWR:** Total NOAA-POES hemispheric power, the estimated power in gigawatts deposited in the polar regions by energetic particles. Measured during transits over the poles by NOAA polar orbiting satellites (*NOAA/POES* [2013]). **[2.2/2.3] BigEv.P/ModEv.P:** GOES Daily Proton Fluence: The daily integrated particle fluxes measured by the primary GOES spacecraft at geosynchronous altitudes for protons of energies > 10 MeV, (ModEv.P) and > 100 MeV (BigEv.P) in units of Protons $\text{cm}^{-2}\cdot\text{day}^{-1}\cdot\text{sr}^{-1}$. (*NOAA/SWPC* [2013]). **[2.4/2.5] BigEv.E/ModEv.E:** GOES Daily Electron Fluence: the daily integrated electron fluxes measured at geosynchronous altitudes by the primary GOES spacecraft for electrons of energies > 0.6 MeV ModEv.E and energies > 2 MeV BigEv.E in units of Electrons $\text{cm}^{-2}\cdot\text{day}^{-1}\cdot\text{sr}^{-1}$. (*NOAA/SWPC* [2013]).

Group 3. This group is composed of 19 terrestrial temperature anomaly data sets. The data sets are monthly data and were interpolated to daily data using a cubic spline. **[3.1 – 3.2] AO, AAO:** Arctic Oscillation, Antarctic Oscillation These “Teleconnection” indices are the largest factors of an Empirical Orthogonal Function expansion of the monthly mean 1000 hPa height anomaly poleward of 20N latitude for the Northern Hemisphere (AO), and of the monthly mean 700 hPa height anomaly poleward of 20 S latitude for the Southern Hemisphere (AAO) (*NWS/CPC*[2013]). **[3.3 – 3.4] North Atlantic Oscillation (NAO), Pacific North American Pattern (PNA).** The NAO and the PNA are defined as the first and second modes of a Rotated Principal Component Analysis applied to monthly standardized 500 mb height anomalies obtained from the Climate Data Assimilation System in the analysis region 20°N – 90°N between January 1950 and December 2000 (*NWS/CPC*[2013A]). **[3.5 – 3.7] Ocean.HA, Ocean.HB, Ocean.HC :** Equatorial upper 300 m temperature average anomalies based on 1981-2010 Climatology for the longitude bands [130°E–80°W], [160°E–80°W], [180°W–100°W] respectively (*NWS/CPC* 2013B). **[3.8 – 3.10] NH.Ocean, SH.Ocean, NS.Ocean :** Ocean Anomaly indices for the latitude bands: [0° – 90°N], [0° – 90°S], [90°S–90°N] re-

spectively. **[3.11 – 3.13] NH.Land, SH.Land, NS.Land** : Land Anomaly indices for the latitude bands $[0^\circ - 90^\circ\text{N}]$, $[0^\circ - 90^\circ\text{S}]$, $[90^\circ\text{S}-90^\circ\text{N}]$ respectively. **[3.14 – 3.16] NH.LO, SH.LO, NS.LO** : Land/Ocean Anomaly indices for the latitude bands $[0^\circ - 90^\circ\text{N}]$, $[0^\circ - 90^\circ\text{S}]$, $[90^\circ\text{S}-90^\circ\text{N}]$ respectively. These 9 data sets [3.8 – 3.16] are from NOAA’s National Climatic Data Center (NOAA/NCDC, 2013). **[3.17] ONI** : Ocean Nino index. The Oceanic Nino Index (ONI) is a three month running mean of NOAA ERSST.v2 SST anomalies in the Nino 3.4 region ($5^\circ\text{N}-5^\circ\text{S}$, $120^\circ-170^\circ\text{W}$), based on the 1971-2000 base period (*NWS/CPC* [2013c]). **[3.18] GIS.TA** : GISS global Land-Ocean temperature index in 0.01 degrees Celsius, using base period 1951 – 1980 (*GISS* [2013]). **[3.19] GLAAM**: globally averaged angular momentum (*NOAA/ESRL* [2013])

Group 4. The LIS/OTD global lightning data sets (*Cecil* [2014]). We used two data sets produced by the LIS/OTD team. The first is the the High Resolution Annual Climatological data set **HRAC**. This is daily average data on a $0.5^\circ \times 0.5^\circ$ grid. The daily data is the climatological average over the years of data (1994 – 2012). The second data set used is the Low Resolution Time Series data, **LRTS**, low resolution daily data for each day from 1994 – 2012. These are daily total flash rate density on a $2.5^\circ \times 2.5^\circ$. These data were summed over 13 regions of the world corresponding to various lightning-producing regions. These regions are shown in Figure 12 along with their Region_IDs.

Group 5. The GPCP global one-degree daily-precipitation data set (PRECIP) GPCP 1degree data *Adler et al*, [2003]. These data were summed over 13 regions of the world corresponding to the various lightning-producing regions shown in Figure 12.

Group 6. Lunar and solar ephemeris data. These time series were computed using the algorithms found at the Orbital Mechanics with MATLAB web site *Eagle* [2013]. The parameters computed were: **[6.1] SD**: Solar Declination, **[6.2] SR**: Solar Distance (AU), and **[6.3] LU**: Lunar Phase angle.

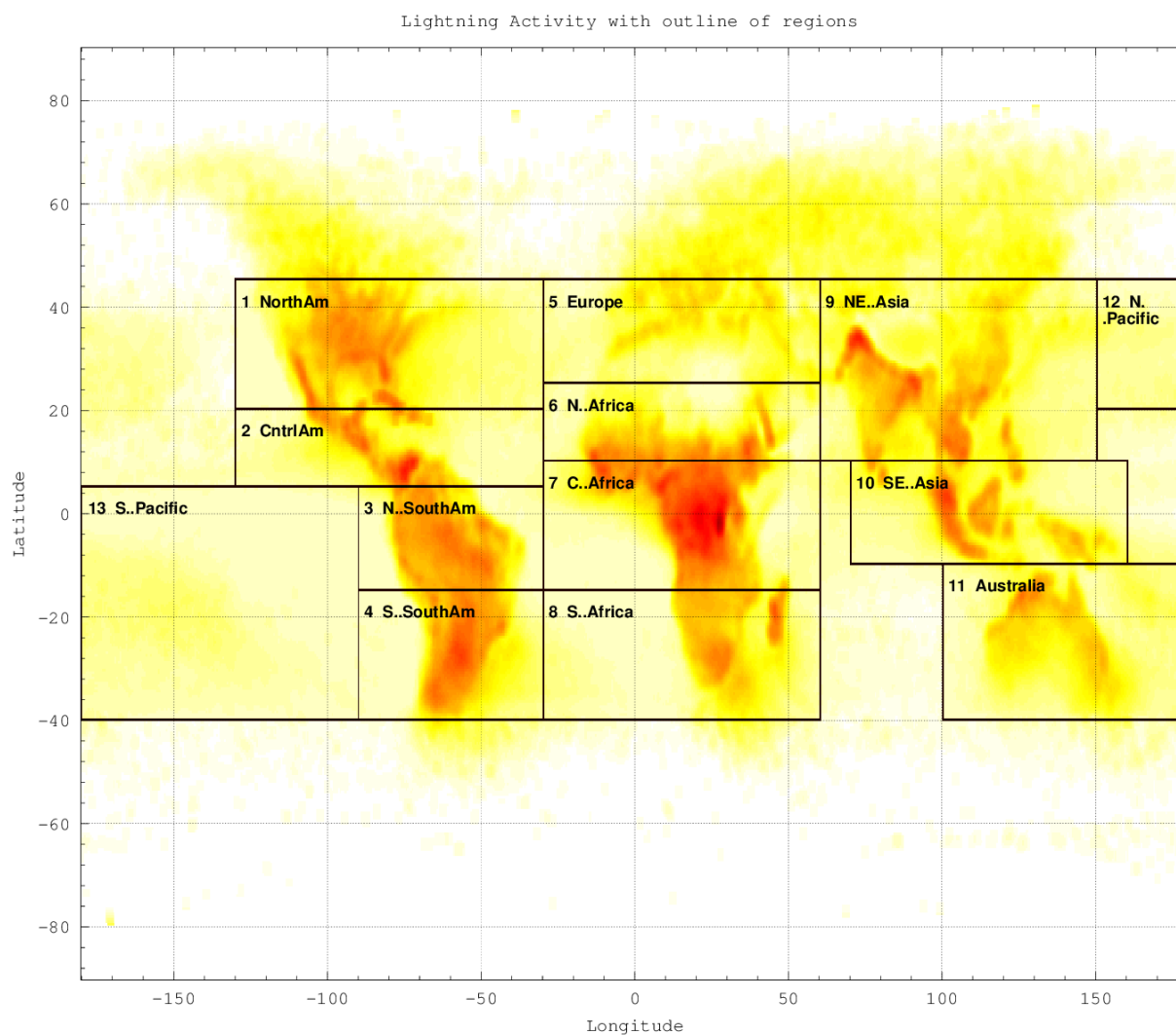


Figure 12: Regions used to compute regional Lightning Rates and Precipitation Rates. Background image shows normalized annual total lightning activity.

PAIRWISE TESTS: CORRELATION AND CAUSALITY

Cross-correlation

Two related tests were performed to assess the magnitude of the various putative influences upon the residual SR time series. The first is the pair-wise correlation between each of the 60 predictors and the 54 predictands. Figure 13 shows the matrix of the 20 highest average cross-correlations between the predictors and predictands. In this Figure, each of 54 columns is one SR parameter. Above the Figure are the labels of the columns, grouped by fit parameter, then mode, then channel. The rows of the Figure are the 20 predictors with the highest average correlation with the 54 predictands. Note that predictors tend to have high correlations with the predictands on either the left side or right side of the matrix. The variable most highly correlated (on average) is **10CM**, the 10.7 cm radio emissions from the Sun. It is most highly correlated with F and Q variations (left side of the matrix) and not correlated with the Intensity variations (right hand side of the matrix).

It can be seen from this matrix that 8 of the top 10 predictors are from either group (1) or (2), where group 1 contains the six direct measures of solar activity, and group 2 contains the five space-weather variables. Note also that these variables are most highly correlated with the fit parameters peak-center frequency (F) and peak-quality factor (Q), on the left side of the matrix, and that they are NOT correlated with the peak intensity (I) on the right hand side of the matrix. Conversely, members from Group 3, the terrestrial temperature anomaly data sets are most highly correlated with the peak intensity (I) on the right hand side of the matrix and NOT with the fit parameters peak-center frequency (F) and peak-quality factor (Q), on the left side of the matrix.

Granger Causality

This analysis does not consider the time ordered nature of the data; consequently, we also performed a pair-wise Granger causality test for each of the 60 predictors and the 54 predictands. In the Granger causality test, we first model the Y data as an auto-regressive process of lag τ $AR(\tau)$. We then test to see if the past values of X can improve this model. If it can, then X is said to “Granger-cause” Y . The Granger-causality model is given in Figure 7 where the value of τ is 1, indicating we consider just one lag.

$$Y(t) = \underbrace{\sum_{\tau=1}^{\tau_{\max}} \alpha_{\tau} Y(t-\tau)}_{\text{Past values of } Y} + \underbrace{\sum_{\tau=1}^{\tau_{\max}} \beta_{\tau} X(t-\tau)}_{\text{Past values of } X} \quad (7)$$

The metric to judge if X Granger-causes Y is the change in the Bayesian information criterion (BIC) when X 's past values are added to the model. The BIC can be defined as:

$$\text{BIC} = -2 \cdot \ln \sigma^2 + k \cdot \ln(n), \quad (8)$$

where k is the number of free parameters in the model, n is the sample size, and σ^2 is the variance of the model. The significance level of changes in BIC (ΔBIC) are discussed in *Kass and Raftery* [1995]. We here consider values in excess of 32 as highly significant.

The results of the pair-wise Granger analysis are shown in Figure 14. We see a result more striking than that found with the cross-correlation analysis in that variables with a direct link to the sun (e.g. **10CM**, **SSN**, **SSA**, **Xray.L**, **Xray.S**) or to space weather **T.PolarPwr** Granger-cause fit parameters peak-center frequency (F) and peak-quality factor (Q), on the left side of the matrix, and that they do NOT Granger-cause the peak intensity (I) on the right hand side of the matrix. In fact none of the tested predictors had significant Granger-causality with the Intensity of the predictands

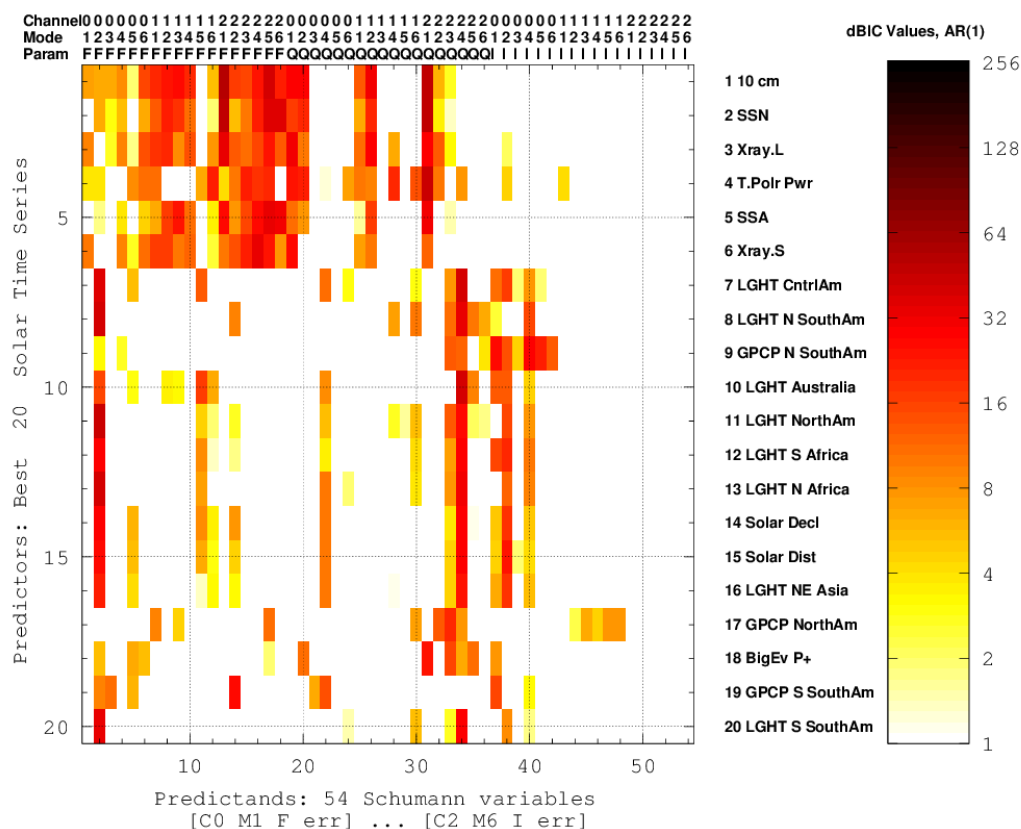


Figure 14: Best 20 predictors based on BIC criterion evaluation of Granger causality Sort order is based on the average BIC criterion over all 54 fitted Lorentzian parameters (F, I, and Q), Channels (E/W, N/S, and Ez) and resonance modes (1 – 6).

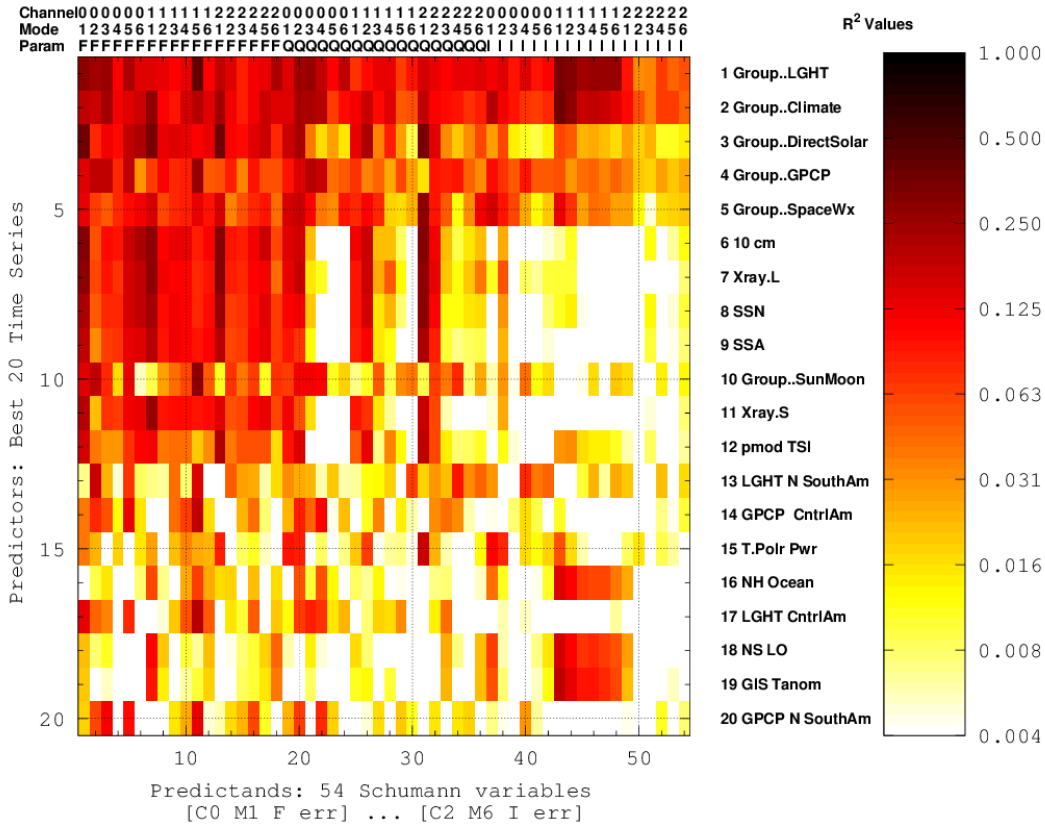


Figure 15: Sorted list of Top 20 R^2 values of multiple predictors, ordinary least square regression. Sort order is based on the average (R^2) over all 54 fitted Lorentzian parameters (F, I, and Q), Channels (E/W, N/S, and Ez) and resonance modes 1 – 6.

GROUP-WIDE ANALYSIS

We also examined the influence that the groups as a whole has upon the predictands via multiple-least squares analyses. The results of this analysis are presented in Figure 15. We find again that the terrestrial temperature anomaly group, the LIS/OTD global lightning group and the GPCP global one-degree daily-precipitation group contribute to the variations of the peak-center frequency, peak-quality factor as well as peak intensity, while the space-weather variables group and the direct measures of solar activity group contribute primarily to the peak-center frequency and peak-quality factor and less so to the peak intensity. The median R^2 between a group and the 54 predictands was 0.12 for both the terrestrial temperature anomaly group and the LIS/OTD global lightning group, 0.06 for GPCP global one-degree daily-precipitation group, the space-weather group, and direct measures of solar activity group, and 0.02 for the lunar and solar ephemeris group.

SPECTRAL ANALYSIS

Due to lightning strikes, electrical-power outages, and other disruptive events, the SR data are characterized as having many data gaps ranging from a hours to months. These data gaps are the equivalent of multiplying the complete data record with an irregular “comb function” that removes the data. We therefore use the “CLEAN algorithm of *Heslop and Dekkers* [2002] based on *Högbom*, [1974] to to examine the spectral characteristics of the 54 residual SR signals. In brief, both the “Frequency” and “Quality-factor” parameters, averaged over all of the SR modes and channels display strong peaks at 180 day, 365 day, and 11 years and a small peak at 27 days that might be associated with the Carrington rotation. In comparison, the “Intensity” parameter displays no similar features, just a roll-off in power with increasing frequency.

Figure 18 shows the average spectra of Lorentzian-fit parameter I, averaged over all Channels (E/W, N/S, Ez), and modes (1 – 6) . Figure 16 and Figure 17 show the corresponding averages of Frequency and Quality-factor. Figure 19 Shows the average spectra of the Lorentzian-fit parameters (F,Q), Channels (E/W, N/S, Ez, and modes (1 – 6) .

The peak could be due to the Space weather variables and/or the Direct Solar variables as Figure 20 shows the average spectra of the Space weather variables, the Direct Solar variables and the climate variables. We note that both the Space weather variables and the Direct Solar variables show peaks in the region of 27 days, and the Space weather variables also show a peak at 13.5 days which can be as strong as the peak at 27 days (*Mursula and Ziegerl* [1966]).

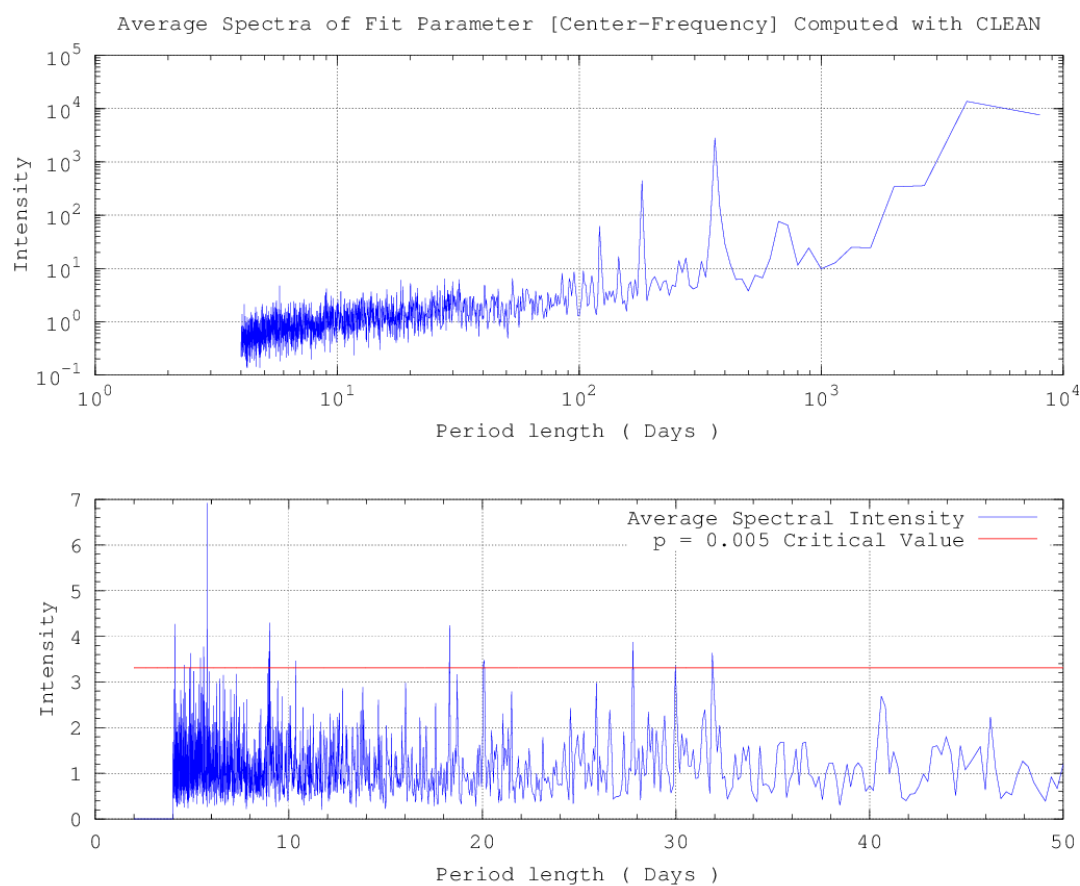


Figure 16: Average spectra of Lorentzian-fit parameter Center-Frequency, averaged over all Channels (E/W, N/S, Ez), and modes 1 – 6.

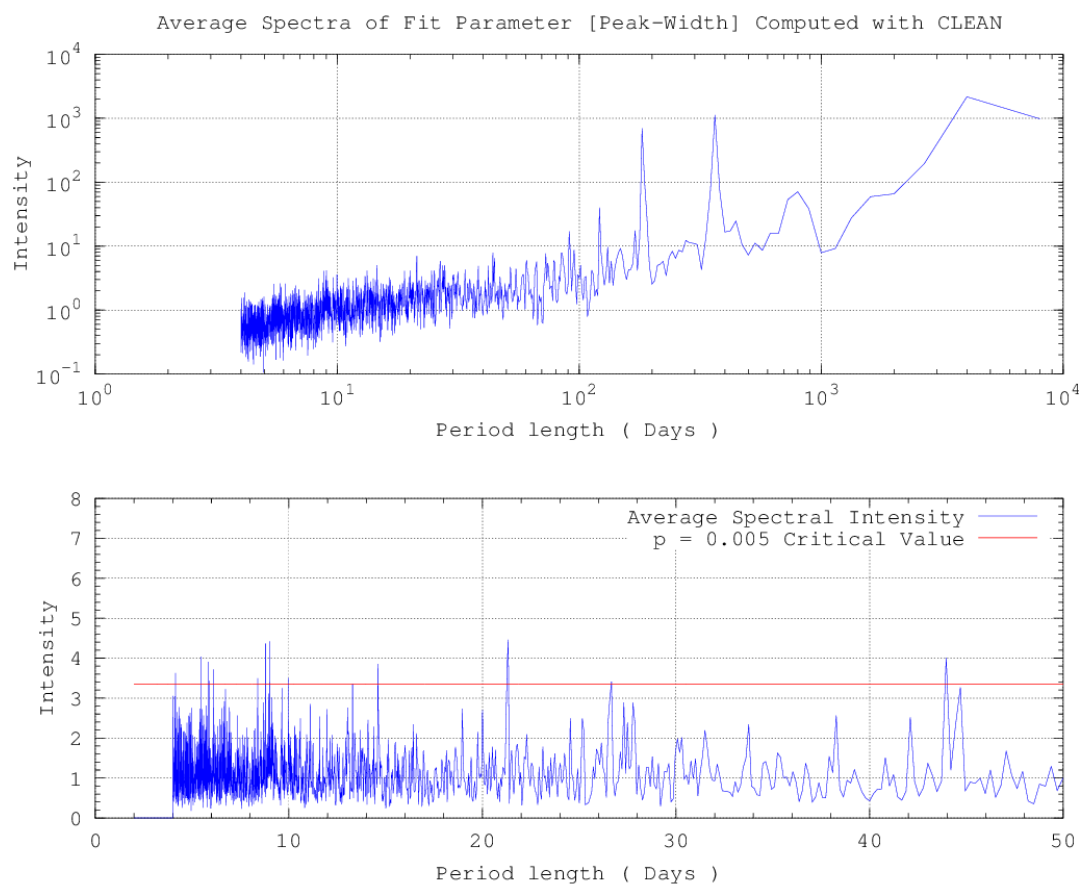


Figure 17: Average spectra of Lorentzian-fit parameter Peak-Width, averaged over all Channels (E/W, N/S, Ez), and modes 1 – 6.

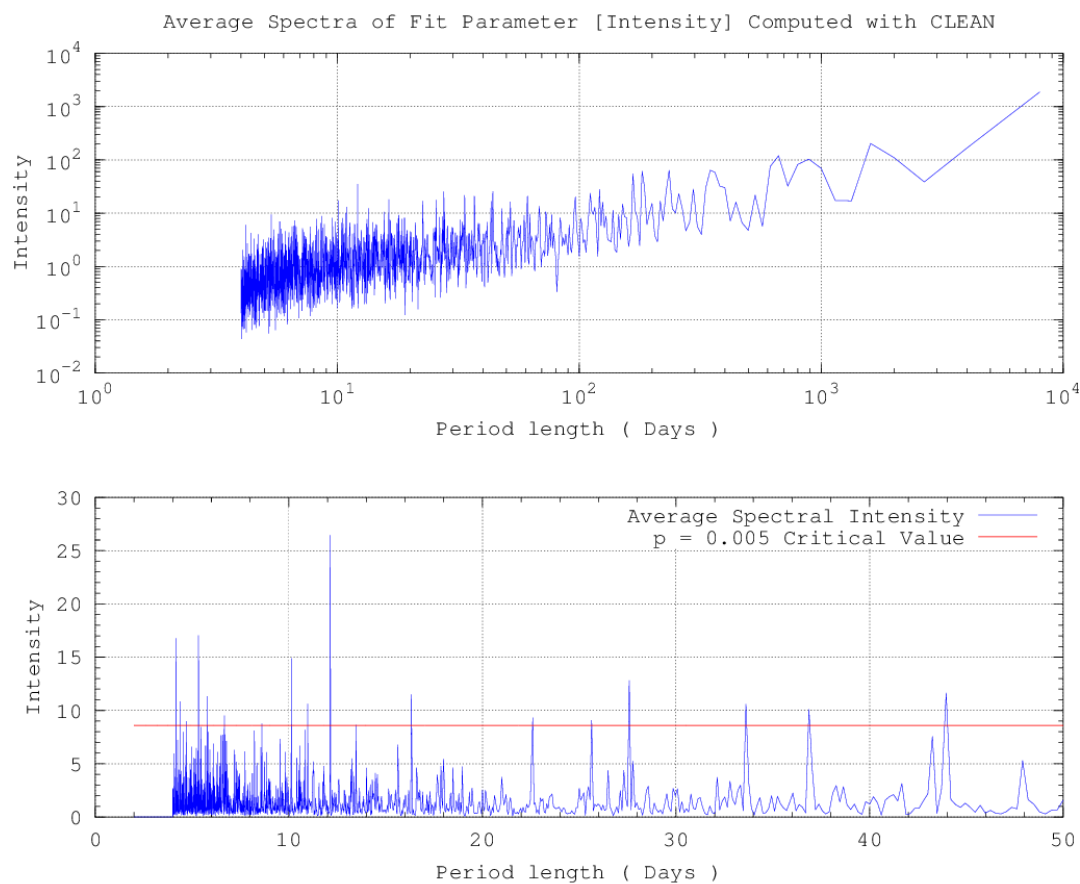


Figure 18: Average spectra of Lorentzian-fit parameter Intensity, averaged over all Channels (E/W, N/S, Ez), and modes 1 – 6.

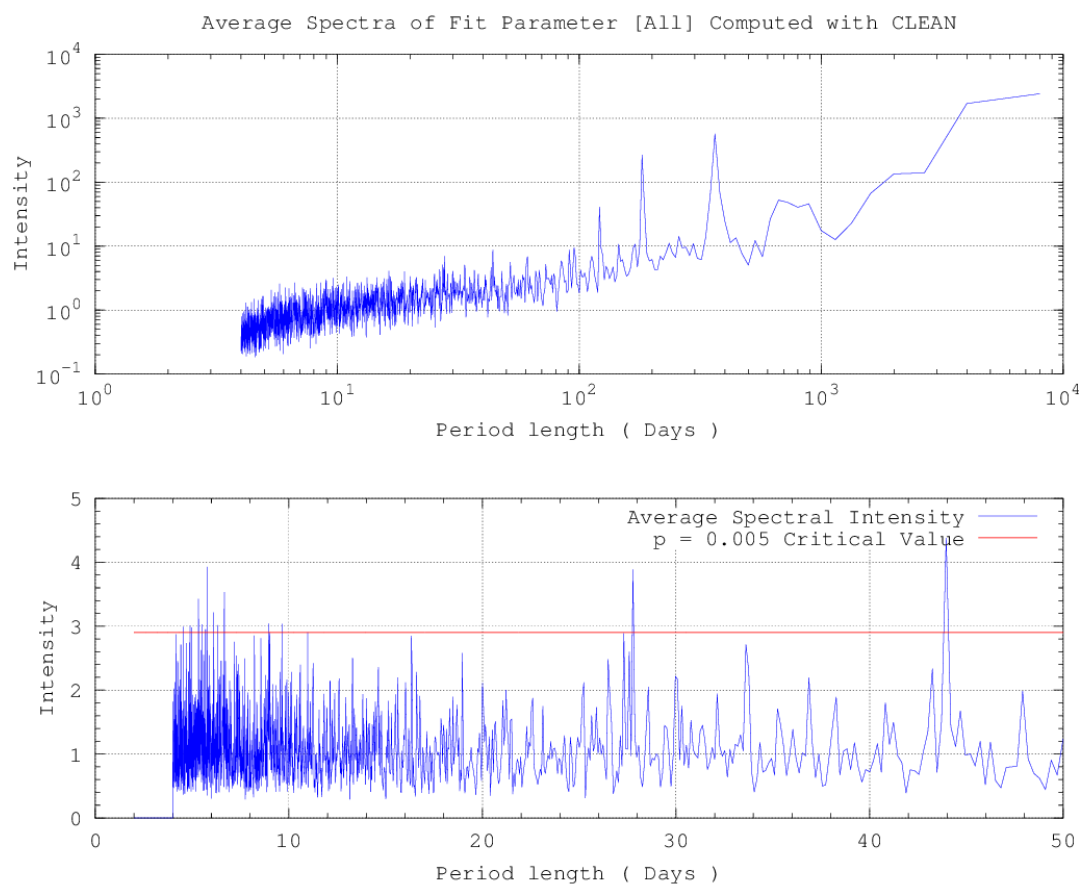


Figure 19: Average spectra of all Lorentzian-fit parameters (Peak-Center Frequency, Peak-Width, and Intensity), Channels (E/W, N/S, Ez, and modes 1 – 6).

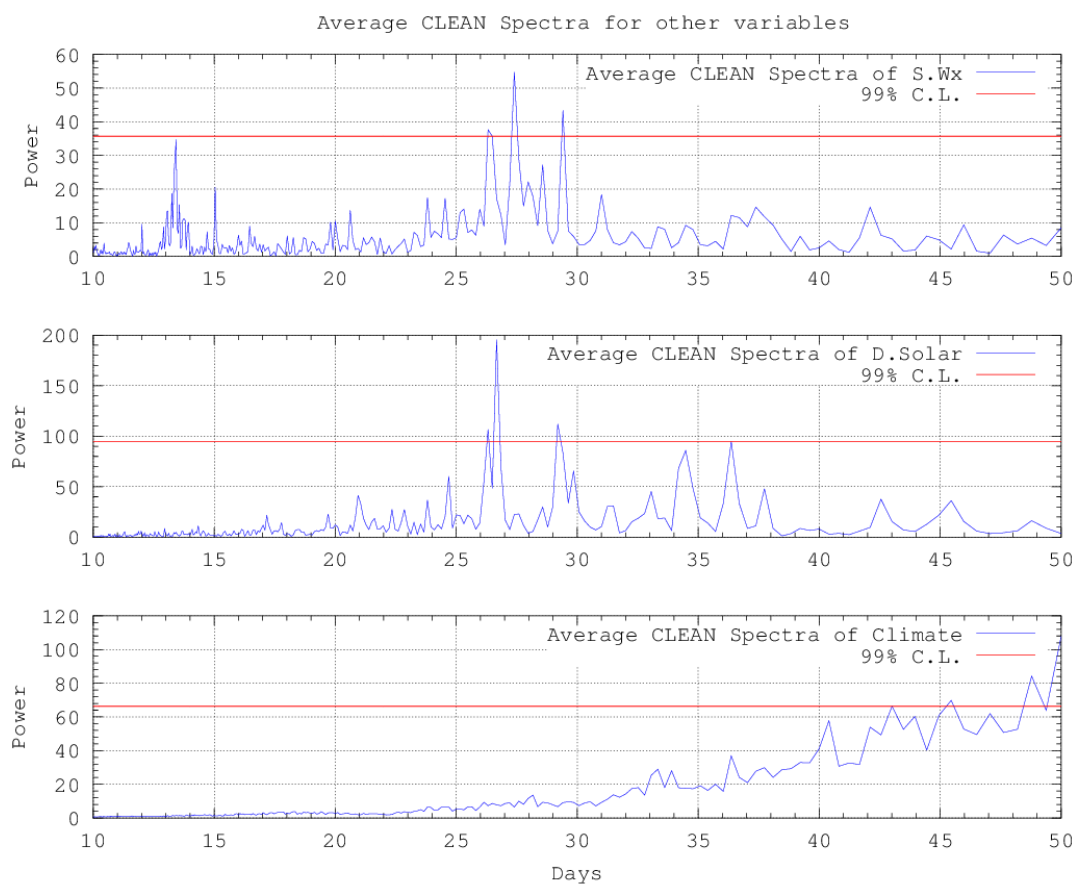


Figure 20: Average spectra of (Top) Space weather variables, (Middle) Direct Solar variables, (bottom) Climate variables. Spectra were computed using the “clean” algorithm.

CONCLUSIONS

Using the LIS/OTD derived HRAC total lightning data set, the uniform cavity model, and the normal mode equations, approximately 50% of the variance in the Rhode Island Schumann data can be accounted for. The sunspot cycle has an effect on values of the peak-center frequency and peak-quality factor parameters but not the peak intensity parameter of the Lorentzian line shape model. The sunspot cycle accounts for approximately 30% of the Of the remaining 50% of the variance unaccounted for by the global lightning data.

Using a variety of techniques, we find that direct measures of solar activity (e.g. sunspot number and area) most strongly influence peak-center frequency and peak-quality factor (median $R^2 = 0.50$) and less so the peak-intensity (median $R^2 = 0.02$). Terrestrial temperature signals (e.g. Ocean temperature anomalies) influence peak-intensity (median $R^2 = 0.15$) but not peak-center frequency nor peak-quality factor (median $R^2 = 0.01$).

We also examined the spectral characteristics of the residual SR signals. Both the peak-center frequency and peak-quality factor parameters, averaged over all of the modes and channels, display strong peaks at 11 years, 365 days, 180 days; in contrast, the peak-intensity parameter displays no similar features. This indicates that the values of the peak intensity parameter are well predicted by the global total lightning and the uniform-cavity model, while the peak-center frequency and peak-quality factor parameters are not. The values of these two parameters have a significant variation over the sunspot cycle unaccounted for by the global total lightning and the uniform-cavity model.

REFERENCES

- Adler, R.F., G.J. Huffman, A. Chang, R. Ferraro, P. Xie, J. Janowiak, B. Rudolf, U. Schneider, S. Curtis, D. Bolvin, A. Gruber, J. Susskind, P. Arkin, E. Nelkin 2003: The Version 2 Global Precipitation Climatology Project (GPCP) Monthly Precipitation Analysis (1979-Present). *J. Hydrometeor.*, **4**, 1147-1167.
- Cecil 2014. Gridded lightning climatology from TRMM-LIS and OTD: *Atmospheric Research*, vol 135, pp 404 - 414. Retrieved from http://thunder.msfc.nasa.gov/data/data_lis-otd-climatology.html on 7 October, 2013.
- Eagle, 2013. Orbital Mechanics with MATLAB web site, maintained by C. David Eagle. <http://www.cdeagle.com/html/ommatlab.html>, retrieved 3 October, 2013.
- GISS, 2013. GISS Land-Ocean temperature anomalies, <http://data.giss.nasa.gov/gistemp/tabledata/GLB.Ts+dSST.txt>, retrieved on 20 October, 2013.
- Heckman, S. J., E. Williams, and B. Boldi (1998), Total global lightning inferred from Schumann resonance measurements, *J. Geophys. Res.*, **103(D24)**, 3177531779, doi:10.1029/98JD02648.
- Heslop and Dekkers, 2002. Spectral analysis of unevenly spaced climatic time series using CLEAN: signal recovery and derivation of significance levels using a Monte Carlo simulation. *Physics of the Earth and Planetary Interiors* **130**, 103116.
- Högbom, J.A. 1974, Aperture synthesis with a non-regular distribution of interferometer baselines, *Astron. Astrophys. Suppl.* **Vol 15**, 417.
- Huang-1998, Electromagnetic Transients, Elves, and Sprites in the Earth-Ionosphere Waveguide, Master of Engineering in Electrical Engineering and Computer Science Thesis, *Massachusetts Institute of Technology*,

Cambridge, Massachusetts, USA, February 1998.

Ishaq, M. and Jones, D. L. (1977). Methods of obtaining radiowave propagation parameters for the earth-ionosphere duct at ELF. *Electronic Letters*, **13**, 9.

Jones, D. L. (1967). Schumann resonances and ELF propagation for inhomogeneous isotropic ionospheric profiles. *Journal of Atmospheric and Terrestrial Physics*, **29**.

Kass, Robert E., R. E. Adrian, 1995. Bayes Factors *Journal of the American Statistical Association*, Vol. 90, No. 430. (Jun., 1995), pp. 773-795.

Mursula, Kalevi, and Bertalan Ziegerl, 1966. The 13.5-day periodicity in the Sun, solar wind, and geomagnetic activity: The last three solar cycles. *JGR*, **101**, No. A12, pp 27,07727,090, December, 1996.

Nickolaenko, A. P., E. I. Yatsevich, A. V. Shvets, M. Hayakawa, and Y. Hobara (2011), Universal and local time variations deduced from simultaneous Schumann resonance records at three widely separated observatories, *Radio Sci.*, **46**, RS5003, doi:10.1029/2011RS004663.

NOAA/ESRL, 2013. Globally averaged angular momentum. <http://www.esrl.noaa.gov/psd/data/correlation/glaam.data.scaled>, retrieved on 3 October 2013.

NOAA/NCDC, 2013. Land and Ocean temperature anomalies, hemispheric and global averages. NOAA's National Climatic Data Center. <ftp://ftp.ncdc.noaa.gov/pub/data/anomalies>, retrieved on 15 October 2013. For a discussion of the origin of these data sets, see <http://www.ncdc.noaa.gov/cmb-faq/anomalies.php>.

NOAA/NGDC, 2013. GOES X-ray data are from The National Geophysical Data Center (NOAA/NGDC), <http://satdat.ngdc.noaa.gov/sem/goes/data/full/xrays>, retrieved 1 Oct 2013.

NOAA/POES, 2013. Total NOAA-POES hemispheric power obtained from U.S. Dept. of Commerce, NOAA, Space Environment Center, <http://www.swpc.noaa.gov/ftpdir/lists/hpi>, retrieved on 2 October 2013.

NOAA/SESC, 2013. Sunspot-number data from the U.S. Dept. of Commerce, NOAA, Space Environment Service Center (SESC), <http://www.swpc.noaa.gov/ftpmenu/warehouse>, 1992-2013.

NOAA/SWPC, 2013A. Sunspot area data obtained from the Daily Solar Data (DSD) files located at the NOAA Space Weather Prediction Center <http://www.swpc.noaa.gov/ftpdir/warehouse>, retrieved 7 October, 2013.

NOAA/SWPC, 2013B Proton and Electron fluences data obtained from the Daily Particle Data (DPD) files located at the NOAA Space Weather Prediction Center <http://www.swpc.noaa.gov/ftpdir/warehouse>, retrieved 7 October, 2013.

NWS/CPC 2013A. AO and AAO indices. NOAA, National Weather Service, Climate Prediction Center. http://www.cpc.ncep.noaa.gov/products/precip/CWlink/daily_ao_index/history/method.shtml, retrieved 5 October, 2013.

NWS/CPC 2013B. Equatorial Upper 300m temperature Average anomaly. NOAA, National Weather Service, Climate Prediction Center. http://www.cpc.ncep.noaa.gov/products/analysis_monitoring/

ocean/index/heat_content_index.txt, retrieved 5 October, 2013.

NWS/CPC, 2013C. http://www.cpc.ncep.noaa.gov/products/analysis_monitoring/ensostuff/ensoyears.shtml, retrieved on 2 October, 2013.

PMOD/WRC, 2013. The Total Solar Irradiance at 1AU, TSI was obtained from Physikalisch-Meteorologisches Observatorium Davos, World Radiation Centre (PMOD/WRC) which contains unpublished data from the VIRGO Experiment on the cooperative ESA/NASA Mission SoHO, retrieved 1 Oct 2013.

Sentman, D.D., 1987. Magnetic elliptical polarization of Schumann resonances. *Radio Science*, **22**, 595606.

Shvets, A. V., Y. Hobara, and M. Hayakawa (2010), Variations of the global lightning distribution revealed from three-station Schumann resonance measurements, *J. Geophys. Res.*, **115**, A12316, doi:10.1029/2010JA015851.

SIDC, 2013. Sunspot number data from the Solar Influences Data Analysis Center (SIDC), World Data Center for the sunspot Index, Royal Observatory of Belgium, Monthly Report on the International sunspot Number, online catalog of the sunspot index.,<http://www.sidc.be/sunspot-data>, 1992-2013.

Wait, J. R. (1996). Electromagnetic Waves in Stratified Media. IEEE Press, Piscataway, NJ. (Derivation of the Normal Mode Equations for E and H.)

Williams, E. R., and G. Stori (2007), Solar radiation-induced changes in ionospheric height and the Schumann resonance waveguide on different timescales, *Radio Sci.*, **42**, RS2S11, doi:10.1029/2006RS003494.

Williams, E. R., V. C. Mushtak, and A. P. Nickolaenko (2006), Distinguishing ionospheric models using Schumann resonance spectra, *J. Geophys. Res.*, **111**, D16107, doi:10.1029/2005JD006944.

Williams, E. R., Lyons, W. A., Hobara, Y., Mushtak, V. C., Asencio, N., Boldi, R., Br, J., Cummer, S. A., Greenberg, E., Hayakawa, M., Holzworth, R. H., Kotroni, V., Li, J., Morales, C., Nelson, T. E., Price, C., Russell, B., Sato, M., Stori, G., Shirahata, K., Takahashi, Y. and Yamashita, K., 2010. Ground-based detection of sprites and their parent lightning flashes over Africa during the 2006 AMMA campaign. *Q.J.R. Meteorol. Soc.*, **136**, 257271. doi: 10.1002/qj.489